Monthly Notices of the ROYAL ASTRONOMICAL SOCIETY

MNRAS **518,** 821–846 (2023) https://doi.org/10.1093/mnras/stac3126
Advance Access publication 2022 October 29

Three-dimensional numerical simulations of ambipolar diffusion in NS cores in the one-fluid approximation: instability of poloidal magnetic field

Andrei P. Igoshev ★ and Rainer Hollerbach
Department of Applied Mathematics, University of Leeds, LS2 9JT Leeds, UK

Accepted 2022 October 25. Received 2022 October 25; in original form 2022 August 1

ABSTRACT

We numerically model evolution of magnetic fields inside a neutron star under the influence of ambipolar diffusion in the weak-coupling mode in the one-fluid MHD approximation. Our simulations are 3D and performed in spherical coordinates. Our model covers the neutron star core and includes crust where the magnetic field decay is due to Ohmic decay. We discover an instability of poloidal magnetic field under the influence of ambipolar diffusion. This instability develops in the neutron star core and grows on a time-scale of 0.2 dimensionless times, reaching saturation by 2 dimensionless times. The instability leads to formation of azimuthal magnetic field with azimuthal wavenumber $m = 14$ (at the moment of saturation) which keeps merging and reaches $m = 4$ by 16 dimensionless times. Over the course of our simulations (16 dimensionless times) the surface dipolar magnetic field decays, reaching 20 per cent of its original value and keeps decaying. The decay time-scale for the total magnetic energy is six dimensionless times. The ambipolar diffusion induces electric currents in the crust where these currents dissipate efficiently. Strong electric currents in the crust lead to heating, which could correspond to luminosities of $\approx 10^{29}$ erg s^{-1} during hundreds of Myrs for an initial magnetic field of 10^{14} G. Ambipolar diffusion leads to formation of small-scale magnetic fields at the neutron star surface.

Key words: magnetic fields – MHD – methods: numerical – stars: magnetic field – stars: neutron.

1 INTRODUCTION

Neutron stars (NSs) are observed as vastly different astrophysical sources of transient and periodic nature which emit electromagnetic radiation ranging from radio to γ-rays. Isolated pulsars are best known for their periodic radio pulses (Lorimer & Kramer 2012); Anomalous X-ray Pulsars and Soft Gamma Repeaters known as magnetars are mostly seen in X-rays and occasionally as transients in γ-rays and radio (for review see Kaspi & Beloborodov 2017). The X-ray Dim Isolated Neutron stars (XDINs; for review see Turolla 2009) and central compact objects (CCOs; for review see Mayer & Becker 2021) emit thermal X-ray radiation only.

It was suggested by Harding (2013) that this observed diversity of NSs is explained by diversity of their magnetic field configurations and evolution. In this framework, magnetars have the strongest poloidal fields with comparable strength crust-confined toroidal fields (see e.g. Igoshev et al. 2021a). Central compact objects might have dipolar magnetic field suppressed by the fall-back (Shabaltas & Lai 2012; Viganò & Pons 2012; Igoshev, Elfritz & Popov 2016) or alternatively only small-scale magnetic fields generated as a result of a stochastic dynamo (Gourgouliatos, Hollerbach & Igoshev 2020; Igoshev et al. 2021c). Similarly, an interpretation of observational properties for XDINs was suggested recently by De Grandis et al. (2021) in the framework of magneto-thermal evolution of NSs (Pons, Miralles & Geppert 2009). Thus, theoretical and computational studies of magnetic field evolution inside NSs is of great importance to decode and put into context NS observations. For a recent review of this problem (see Igoshev, Popov & Hollerbach 2021b).

NS magnetic field evolution is driven by Ohmic decay, Hall effect, ambipolar diffusion (Goldreich & Reisenegger 1992), and by effects related to superconductivity in the NS core (Glampedakis, Andersson & Samuelsson 2011; Graber et al. 2015), see also recent work by Wood & Graber (2022). The magnetic field evolution is coupled to the thermal evolution (Pons et al. 2009). Some of these effects are studied reasonably well via analytical and numerical efforts. The magnetic field evolution driven by Ohmic decay and Hall effect in the NS crust was studied extensively by different groups in two and three dimensions (Hollerbach & Rüdiger 2002, 2004; Wareing & Hollerbach 2009, 2010; Gourgouliatos et al. 2013, 2020; Viganò et al. 2013; Gourgouliatos & Cumming 2014, 2015; Gourgouliatos, Wood & Hollerbach 2016; Gourgouliatos & Hollerbach 2018; Igoshev et al. 2021a,c; Anzuini et al. 2022). Most of these efforts were nicely summarized in the recent review by Pons & Viganò (2019).

★ E-mail: ignotur@gmail.com, a.igoshev@leeds.ac.uk

Ambipolar diffusion and superconductivity are less studied. Ambipolar diffusion could be one of the main drivers for evolution of magnetars with internal fields as strong as 5×10^{14}–10^{15} G. Under the influence of ambipolar diffusion their magnetic field will evolve on Myr time-scales. Alternatively, radio pulsars become recycled in low-mass X-ray binaries due to accretion from the secondary star. These NSs become millisecond radio pulsars (MSPs). They are known for their significantly smaller magnetic fields, around 10^8–10^9 G (for review see e.g. Bhattacharya & van den Heuvel 1991). These small magnetic fields might be related to the accretion process (Alpar et al. 1982) or produced as a result of ambipolar diffusion (Cruces, Reisenegger & Tauris 2019).

Ambipolar diffusion is a dynamic process in the NS core which requires the presence of both charged (electrons and protons) and neutral (neutrons) particles. Charged particle motion is mostly driven by electromagnetic fields while neutral particle motion is defined mostly by the NS gravitational potential. Simultaneously, two nuclear reactions take place: (1) neutrons decay into protons and electrons, and (2) protons and electrons merge into neutrons. Rates of these reactions differ for different depths inside the NS core.

In this research, we do not take into account effects of superfluidity and superconductivity. We plan to slowly increase the complexity of our simulations, distinguishing effects related to each individual process. As opposed to the superfluidity and superconductivity in the NS core, the ambipolar diffusion is theoretically understood reasonably well. Thus, meaningful 3D numerical simulations are possible. The addition of superconductivity and superfluidity lead to contradictory conclusions. On the one hand, Elfritz et al. (2016) used the formalism developed by Glampedakis et al. (2011) and found that dissipation and expulsion in the NS core are weak, and thus strong magnetic fields in the core should survive for a long time. On the other hand, Dommes & Gusakov (2017) found that core magnetic field should be expelled on much shorter time-scales due to buoyancy of proton vortices.

Studies of ambipolar diffusion were pioneered by Hoyos, Reisenegger & Valdivia (2008), who established a general multifluid formalism and estimated relevant time-scales in one dimension. They also performed first numerical simulations in the non-linear regime. Later on, Castillo, Reisenegger & Valdivia (2017) developed numerical simulations in spherical coordinates with axial symmetry, i.e. 2D simulations. They adopted an approximation of motionless neutrons and considered the weak coupling mode. Castillo et al. (2017) found that on short time-scales the density of charged particles is perturbed by the ambipolar diffusion velocity in such a way that they create a pressure gradient which cancels the irrotational part of the magnetic force. Thus, the velocity field becomes solenoidal. This solenoidal velocity field drives longer evolution which converges to an equilibrium state. In this equilibrium state, the toroidal magnetic field is confined to regions where the poloidal magnetic field lines are closed (Castillo et al. 2017).

Later on, Passamonti et al. (2017) performed numerical simulations of ambipolar diffusion in two dimensions in the one-fluid approximation. They studied short-term evolution when perturbations in number density of non-charged particles are formed as a response to the Lorentz force affecting the charged particles. They studied formation of these regular perturbations and resulting ambipolar velocity field as a function of NS core temperature. They found that in the weak coupling regime the chemical gradient partly cancels the Lorentz force. It means that the velocity field becomes solenoidal-dominated below 4×10^8 K. Passamonti et al. (2017) found that typical speeds of ambipolar diffusion are km Myr^{-1} in the normal matter case and much faster, 10^3 km Myr^{-1}, in the superconducting case. In the case of superconductivity/superfluidity, the suppression of the irrotational component occurs at higher temperatures below 9×10^8 K. Passamonti et al. (2017) did not model the long-term evolution of magnetic fields nor the influence of neutron star crust.

Recently, Castillo, Reisenegger & Valdivia (2020) performed 2D simulations in the two-fluid approximation with inclusion of neutron motion. In these simulations, they also found that magnetic field evolves toward the 'Grad–Shafranov' equilibria. The behaviour of ambipolar diffusion in three dimensions is expected to differ from two dimensions because multiple instabilities are known for axisymmetric magnetic fields in three dimensions (see e.g. Tayler 1973; Markey & Tayler 1973).

The aim of our article is to model ambipolar diffusion in the weak coupling mode in three dimensions to study if it leads to formation of non-axisymmetric structures. Essentially, we want to check if in three dimensions the ambipolar diffusion leads to an equilibrium state as it was found in axisymmetric simulations (Castillo et al. 2020), or alternatively leads to complete decay of magnetic field. We formulate a set of equations mostly following works by Goldreich & Reisenegger (1992) and Passamonti et al. (2017). In comparison to that work we assume a presence of weak magnetic field decay in the core caused by Ohmic losses, and we include the NS crust in our calculations. We solve the magnetic induction equation and equation for deviation from the β-equilibrium in three dimensions in spherical coordinates using novel spectral code `Dedalus`[1] (Lecoanet et al. 2019; Vasil et al. 2019; Burns et al. 2020).

2 MAGNETIC FIELD EVOLUTION

2.1 Key assumptions

A few different approaches were suggested to simplify the system of equations describing the ambipolar diffusion. The recent notable cases include Castillo et al. (2020) and Passamonti et al. (2017). We mostly follow the prescription by Passamonti et al. (2017) with a few small changes. Here, we summarize our key assumptions and show how they differ from the more recent equation set presented by Castillo et al. (2020).

Similarly to Castillo et al. (2020), we aim at studying the evolution of sequential magnetohydrostatic quasi-equilibrium states. In each of these states, all forces applied to a fluid element are close to balancing each other. Each of these states is reached within a few Alfvén

[1] https://dedalus-project.org

time-scales i.e. within a few seconds of real time. The evolution of magnetic field proceeds on much longer time-scales, 10^2–10^{10} yr. We therefore do not follow the propagation of sound waves, gravity waves, or Alfvén waves.

Unlike Castillo et al. (2020), we neglect inertial terms in the continuity equation for particle densities. Moreover, we also neglect the advective term (baryon velocity), i.e. we assume that total $n_{\rm n}\vec{v}_{\rm n} = -n_{\rm p}\vec{v}_{\rm p}$. Overall, we work in the one-fluid MHD limit similarly to Passamonti et al. (2017). As noted by Castillo et al. (2020), this assumption might lead to underestimation of the time-scale for ambipolar diffusion. In this work, we are more interested in relaxing the axial symmetry assumption which was made in all previous simulations on this topic. In future work, we plan to add equations describing the independent motion of the neutral component.

2.2 Detailed derivation of equations

Following the derivations by Goldreich & Reisenegger (1992) and Passamonti et al. (2017), we begin with the Maxwell–Faraday equation:

$$\frac{\partial \vec{B}}{\partial t} = -c\vec{\nabla}\times\vec{E}, \tag{1}$$

where $\vec{B}$ and $\vec{E}$ are the magnetic and electric fields, and c is the speed of light. In this work, we assume that electric field evolves only under the influence of Ohmic decay and ambipolar diffusion (so keeping the first two terms in equation 6 of Passamonti et al. 2017):

$$\vec{E} = \frac{\vec{j}}{\sigma} - \frac{1}{c}\vec{v}_{\rm p}\times\vec{B}, \tag{2}$$

where σ is the electric conductivity, $\vec{v}_{\rm p}$ is the speed of protons, and $\vec{j}$ is the electric current density:

$$\vec{j} = en_{\rm c}(\vec{v}_{\rm p} - \vec{v}_{\rm e}) = \frac{c}{4\pi}\vec{\nabla}\times\vec{B}, \tag{3}$$

where e is elementary charge, and $n_{\rm c}$ is the number density of charged particles. It is assumed that the number densities of protons and electrons are equal $n_{\rm c} = n_{\rm e} \approx n_{\rm p}$ due to the electroneutrality.

Combining equations (1), (2), and (3) we derive:

$$\frac{\partial \vec{B}}{\partial t} = -\frac{c^2}{4\pi}\vec{\nabla}\times\left(\frac{1}{\sigma}\vec{\nabla}\times\vec{B}\right) + \vec{\nabla}\times(\vec{v}_{\rm p}\times\vec{B}). \tag{4}$$

Now, we replace $\vec{B} = \vec{\nabla}\times\vec{A}$ where $\vec{A}$ is the vector potential:

$$\vec{\nabla}\times\frac{\partial \vec{A}}{\partial t} = -\frac{c^2}{4\pi}\vec{\nabla}\times\left(\frac{1}{\sigma}\vec{\nabla}\times(\vec{\nabla}\times\vec{A})\right) + \vec{\nabla}\times\left[\vec{v}_{\rm p}\times(\vec{\nabla}\times\vec{A})\right]. \tag{5}$$

Taking the 'inverse curl' of this then yields:

$$\frac{\partial \vec{A}}{\partial t} = -\frac{c^2}{4\pi\sigma}\vec{\nabla}\times(\vec{\nabla}\times\vec{A}) + \vec{v}_{\rm amb}\times(\vec{\nabla}\times\vec{A}). \tag{6}$$

Here, similarly to Passamonti et al. (2017) we expand $\vec{v}_{\rm p} = \vec{v}_{\rm b} + x_n(\vec{v}_{\rm p} - \vec{v}_{\rm n})$. In this expression, $x_{\rm n}$ is the neutron fraction and $\vec{v}_{\rm b}$ is the speed of baryons. Further, we assume that baryon speed is negligible and thus we replace $\vec{v}_{\rm p} \approx x_{\rm n}(\vec{v}_{\rm p} - \vec{v}_{\rm n}) = \vec{v}_{\rm amb}$.

The velocity of ambipolar diffusion is written the same way as Passamonti et al. (2017) (see Appendix A for more details):

$$\frac{1}{4\pi n_{\rm c}}(\vec{\nabla}\times\vec{B})\times\vec{B} - \vec{\nabla}(\Delta\mu) = \frac{1}{x_{\rm n}^2}\frac{m_{\rm p}^*\vec{v}_{\rm amb}}{\tau_{\rm pn}}, \tag{7}$$

where $\Delta\mu$ is the deviation from the β-equilibrium, $m_{\rm p}^*$ is the effective proton mass, and $\tau_{\rm pn}$ is the relaxation time for collision between protons and neutrons. We rewrite this equation using the vector potential:

$$\vec{v}_{\rm amb} = \frac{x_{\rm n}^2\tau_{\rm pn}}{4\pi n_{\rm c}m_{\rm p}^*}\left[\left\{\vec{\nabla}\times(\vec{\nabla}\times\vec{A})\right\}\times(\vec{\nabla}\times\vec{A}) - 4\pi n_{\rm c}\vec{\nabla}(\Delta\mu)\right]. \tag{8}$$

Equation (6) is written as

$$\frac{\partial \vec{A}}{\partial t} = -\frac{c^2}{4\pi\sigma}\vec{\nabla}\times(\vec{\nabla}\times\vec{A}) + \frac{x_{\rm n}^2\tau_{\rm pn}}{4\pi n_{\rm c}m_{\rm p}^*}\left[\vec{\nabla}\times(\vec{\nabla}\times\vec{A})\times(\vec{\nabla}\times\vec{A}) - 4\pi n_{\rm c}\vec{\nabla}(\Delta\mu)\right]\times(\vec{\nabla}\times\vec{A}). \tag{9}$$

This is the first of two coupled equations. The second equation determines the deviation from the β-equilibrium. We derive this equation by taking the divergence of equation (7). We provide more details in Appendix A. This equation is written as

$$\vec{\nabla}^2(\Delta\mu) = \frac{m_{\rm p}^*\lambda}{x_{\rm n}^2 n_{\rm c}\tau_{\rm pn}}\Delta\mu + \vec{\nabla}\cdot\left(\frac{1}{4\pi n_{\rm c}}(\vec{\nabla}\times\vec{B})\times\vec{B}\right) - \frac{x_{\rm n}\tau_{\rm pn}n_{\rm c}}{m_{\rm p}^*}\left(-\vec{\nabla}(\Delta\mu) + \frac{1}{4\pi n_{\rm c}}(\vec{\nabla}\times\vec{B})\times\vec{B}\right)\cdot\vec{\nabla}\left(\frac{m_{\rm p}^*}{x_{\rm n}n_{\rm c}\tau_{\rm pn}}\right). \tag{10}$$

We simplify this equation by expanding brackets in the third term on the right side. We also assume that $m_{\rm p}^*$ is constant over the core and $x_{\rm n}n_{\rm c}\tau_{\rm pn}$ only varies in the radial direction. In this case, the equation is written as

$$\vec{\nabla}^2(\Delta\mu) = \frac{m_{\rm p}^*\lambda}{x_{\rm n}^2 n_{\rm c}\tau_{\rm pn}}\Delta\mu + \vec{\nabla}\cdot\left(\frac{1}{4\pi n_{\rm c}}(\vec{\nabla}\times\vec{B})\times\vec{B}\right) - \frac{x_{\rm n}\tau_{\rm pn}}{4\pi}\left(\left\{\vec{\nabla}\times\vec{B}\right\}\times\vec{B}\right)\cdot\frac{\rm d}{{\rm d}r}\left(\frac{1}{x_{\rm n}n_{\rm c}\tau_{\rm pn}}\right) + x_{\rm n}\tau_{\rm pn}n_{\rm c}\frac{\partial\Delta\mu}{\partial r}\frac{\rm d}{{\rm d}r}\left(\frac{1}{x_{\rm n}n_{\rm c}\tau_{\rm pn}}\right). \tag{11}$$

Table 1. Value of numerical coefficients involved in the problem. Top part of the table is for fixed coefficients and constants while the bottom part contains derived coefficients.

Symbol	Eq.	Meaning	Fixed value	Units
		Fixed values		
B_0		Magnetic field strength	1.00×10^{14}	$G = \mathrm{g}^{1/2}\ \mathrm{cm}^{-1/2}\ \mathrm{s}^{-1}$
T_0		Core temperature	1.00×10^{8}	K
$R_{\rm NS}$		NS radius	1.26×10^{6}	cm
$R_{\rm core}/R_{\rm NS}$		Fraction of core to total NS radius	0.925	Dimensionless
t_0		Timescale to make equations dimensionless	10.00	Myr
$m_{\rm p}^*$		Effective proton mass	1.25×10^{-24}	g
s		Relative conductivity of the core	5.00×10^{-3}	Dimensionless
$t_{\rm crust}$		Timescale of Ohmic decay in the crust	30.00	Myr
$\rho_0 = \rho(0)$		Central NS density	7.64×10^{14}	$\mathrm{g\ cm}^{-3}$
$n_{\rm c}^0 = n_{\rm c}(0)$		Number density of charged particles in NS centre	3.30×10^{37}	cm^{-3}
ρ_1		Typical NS density	2.8×10^{14}	$\mathrm{g\ cm}^{-3}$
		Intermediate and diagnostic values		
$\tau_{\rm pn}^0$	16	Relaxation time for collisions	2.97×10^{-17}	s
λ_0	19	mUrca reaction rates	9.76×10^{27}	$\mathrm{erg}^{-1}\ \mathrm{cm}^{-3}\ \mathrm{s}^{-1}$
μ_0	22	Chemical potential	1.38×10^{-8}	erg
$t_{\rm amb}$	20	Timescale of ambipolar diffusion	87.61	Myr
$v_{\rm amb,\,0}$	21	Speed of ambipolar diffusion	0.14	$\mathrm{km\ Myr}^{-1}$
σ_0	27	Electrical conductivity for t_0	1.43×10^{22}	s^{-1}
ϵ_0^{ν}	60	Volumetric energy release rate	2.52×10^{12}	$\mathrm{erg\ cm}^{-3}\ \mathrm{s}^{-1}$
ϵ_0	62	Thermal luminosity	5×10^{30}	$\mathrm{erg\ s}^{-1}$
		Dimensionless numerical coefficients of partial differential equations		
Am	26		0.11	Dimensionless
K	23		573.0	Dimensionless
d_1	33		1.97×10^{-5}	Dimensionless

2.3 Neutron star physics

To construct an NS model, we solve numerically the Tolman–Oppenheimer–Volkoff equation (Oppenheimer & Volkoff 1939) using numerical fits to the equation of state developed by Pearson et al. (2018). We use the BSk24 equation from a FORTRAN module.[2] In our calculations, we assume the central pressure of 10^{35} dyn cm^{-2}, which corresponds to an NS with total mass of 1.46 $\mathrm{M}_{\odot}$, radius $R_{\rm NS} = 12.56$ km, and crust depth $h = 0.95$ km. Thus the core–crust transition occurs at radial distance 0.925 $R_{\rm NS}$.

The number density $n_{\rm c}$ of charged particles is computed as

$$n_{\rm c} = Y_{\rm e} x_{\rm n}, \tag{12}$$

where $Y_{\rm e}$ is the fraction of electrons and $x_{\rm n}$ is the baryon number density. The neutron fraction $x_{\rm n}$ is computed as

$$x_{\rm n} = 1 - 2(Y_{\rm e} + Y_{\mu}), \tag{13}$$

where Y_{μ} is the fraction of muons. We subtract two times the electron fraction to remove the proton fraction. We compute relaxation times $\tau_{\rm pn}$ and $\tau_{\rm en}$ using equations provided by Yakovlev & Shalybkov (1990):

$$\frac{1}{\tau_{\rm ep}} = 2.1 \times 10^{16}\ T_9^2 \left(\frac{\rho_1}{\rho}\right)^{5/3}\ \mathrm{s}^{-1}, \tag{14}$$

where $\rho_1 = 2.8 \times 10^{14}$ g cm^{-3}. A similar equation is used to compute the $\tau_{\rm pn}$:

$$\frac{1}{\tau_{\rm pn}} = 4.7 \times 10^{18}\ T_9^2 \left(\frac{\rho_1}{\rho}\right)^{1/3}\ \mathrm{s}^{-1}. \tag{15}$$

We compute the numerical value in Table 1 as

$$\tau_{\rm pn}^0 = 2.13 \times 10^{-19} T_9^{-2} \left(\frac{\rho_0}{\rho_1}\right)^{1/3}\ \mathrm{s}. \tag{16}$$

[2] http://www.ioffe.ru/astro/NSG/BSk/index.html

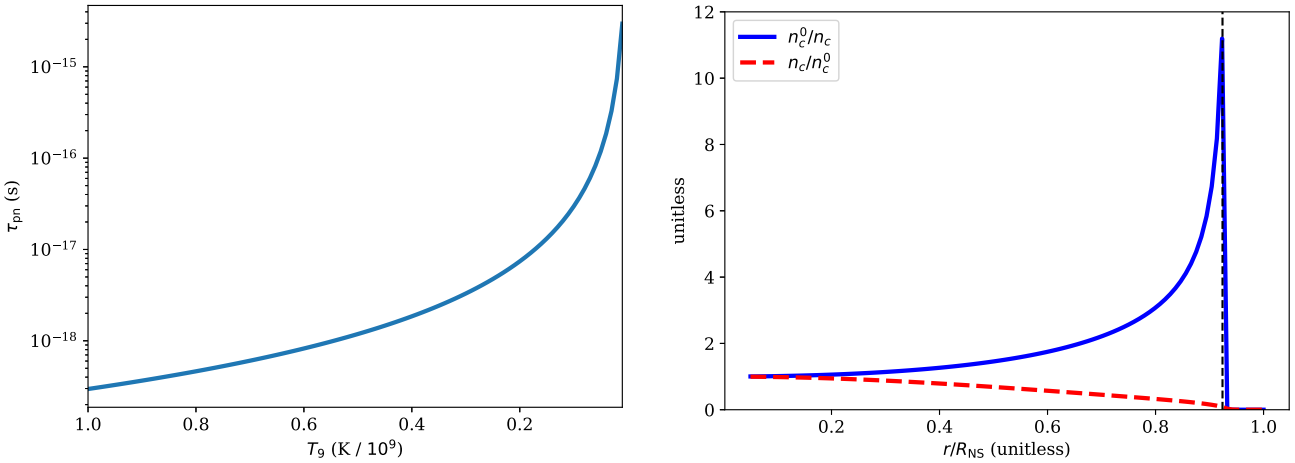

Figure 1. Left-hand panel: τ_{pn} as a function of temperature. The temperature axis is reversed to highlight the fact that NS cools down with time and so moves from left to right. Right-hand panel: profile of number density of charged particles n_c and its inverse in the NS core. Dashed black line shows the crust–core boundary.

The electrical conductivity of the core is computed as

$$\sigma = \frac{e^2 n_c \tau_{pe}}{m_e^*}, \tag{17}$$

where the effective electron mass is computed as $m_e^* = m_e\sqrt{1+x_e^2}$, where x_e is the ratio between the Fermi momentum and the rest mass of the electron m_e. We obtain x_e from the same FORTRAN code `bskfit18.f`. For the effective proton mass, we assume $m_p^* = 0.75 m_p$ throughout the entire NS.

We use the following formalism to describe the change in reaction rate as a function of the deviation from the chemical equilibrium. We introduce λ which is the change of reaction rate depending on deviation from chemical equilibrium $\lambda = (\mathrm{d}\Gamma/\mathrm{d}\Delta\mu)|_{eq}$. We use the equation for the λ factor by Sawyer (1989) similarly to Passamonti et al. (2017):

$$\lambda = 5\times10^{27}\, T_8^6 \left(\frac{\rho}{\rho_1}\right)^{2/3} \ \mathrm{erg^{-1}\ cm^{-3}\ s^{-1}} = \lambda_0 \left(\frac{\rho}{\rho_0}\right)^{2/3}, \tag{18}$$

where λ_0 is computed as

$$\lambda_0 = 5\times10^{33}\, T_9^6 \left(\frac{\rho_0}{\rho_1}\right)^{2/3} \ \mathrm{erg^{-1}\ cm^{-3}\ s^{-1}}. \tag{19}$$

2.4 Time-scale and dimensionless version of the equations

The natural time-scale to consider in this problem is given by (Goldreich & Reisenegger 1992)

$$t_{amb} = \frac{R_{ns}}{\langle v_{amb}\rangle} = \frac{4\pi n_c m_p^* R_{ns}^2}{\tau_{pn} B^2}. \tag{20}$$

In order to estimate this time-scale for some typical values we have to fix temperature (τ_{pn} is very sensitive to temperature, see Fig. 1) and magnetic field strength. For typical parameters summarized in Table 1 we obtain $t_{amb} \approx 90$ Myr. To simulate magnetars we thus introduce dimensionless time $t' = t/t_0$ where $t_0 = 10^7$ yr. It is worth noting that we estimate t_{amb} for the core centre, while for more external regions this time-scale is significantly shorter due to decreasing n_c, see Fig. 1. During the first 10 Kyr of magnetar evolution the time-scale of ambipolar diffusion is large because τ_{pn} is very small due to high interior temperature. For normal radio pulsars with magnetic field $B \approx 5\times10^{12}$ G, the time-scale for ambipolar diffusion is $t_{amb} \approx 32$ Gyr.

We write the equations in dimensionless form beginning with equation (8). The ambipolar velocity $\vec{v}_{amb}$ is one of the key diagnostic variables which shows how ambipolar diffusion proceeds. In axisymmetric simulations, Castillo et al. (2020) it was found that $\vec{v}_{amb}$ decreases by many orders of magnitude at t_{amb} because the configurations approach an equilibrium. To write equation (8) in dimensionless form, we introduce three auxiliary variables:

$$v_{amb,0} = \frac{\tau_{pn}^0 B_0^2}{4\pi n_c^0 m_p^* R_{NS}}, \tag{21}$$

$$\mu_0 = k_B T_0, \tag{22}$$

$$\mathrm{K} = \frac{4\pi\mu_0 n_c^0}{B_0^2}. \tag{23}$$

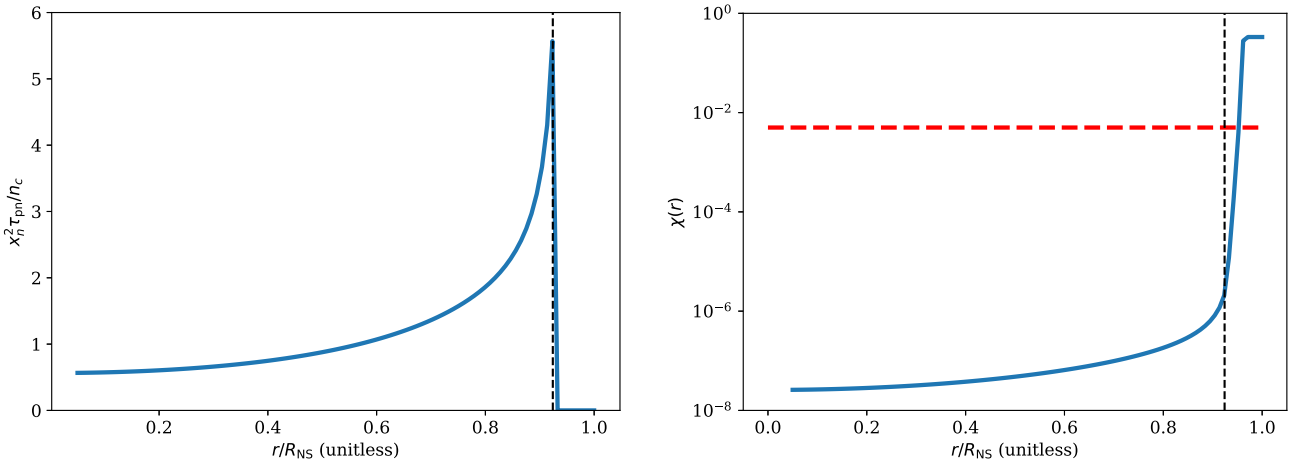

Figure 2. Left-hand panel: radial profile of numerical coefficient determining the speed of ambipolar diffusion. Right-hand panel: radial profile for relative conductivity χ (solid blue line) and additional conductivity s (dashed red line). Dashed black line shows the crust–core boundary.

Thus equation (8) becomes:

$$\vec{v}_{\rm amb} = v_{\rm amb,0}\frac{x_{\rm n}^2\tau_{\rm pn}}{n_{\rm c}}\left[\left\{\vec{\nabla}\times(\vec{\nabla}\times\vec{A})\right\}\times(\vec{\nabla}\times\vec{A}) - {\rm K}n_{\rm c}\vec{\nabla}(\Delta\mu)\right]. \tag{24}$$

The current dimension of this quantity is cm s^{-1}, but for convenience it could also be computed in km Myr^{-1} as in Table 1. Truly dimensionless velocity is:

$$v = v_{\rm amb,0}\frac{t_0}{R_{\rm NS}}. \tag{25}$$

At the next stage, we consider equation (9). The dimensionless version of this equation will contain:

$${\rm Am} = \frac{\tau^0_{\rm pn}t_0B_0^2}{4\pi n_c^0 m_{\rm p}^* R_{\rm NS}^2} = v_{\rm amb,0}\frac{t_0}{R_{\rm NS}}, \tag{26}$$

i.e. our new dimensionless coefficient has meaning of dimensionless velocity of ambipolar diffusion. If we assume that our t_0 corresponds to some fictional conductivity σ_0 via:

$$t_0 = \frac{4\pi\sigma_0 R_{\rm NS}^2}{c^2}, \tag{27}$$

we can also simplify the first term on the right side of equation (9) by introducing a coefficient with profile:

$$\chi(r) = \frac{\sigma_0}{\sigma(r)}. \tag{28}$$

Using these variables, we rewrite equation (9) as

$$\frac{\partial\vec{A}}{\partial t} = -\chi(r)\vec{\nabla}\times(\vec{\nabla}\times\vec{A}) + {\rm Am}\frac{x_{\rm n}^2\tau_{\rm pn}}{n_{\rm c}}\left[\left\{\vec{\nabla}\times(\vec{\nabla}\times\vec{A})\right\}\times(\vec{\nabla}\times\vec{A}) - {\rm K}n_{\rm c}\vec{\nabla}(\Delta\mu)\right]\times(\vec{\nabla}\times\vec{A}). \tag{29}$$

We also take into account that $A_0 = R_{\rm NS}B_0$. In order to solve this equation with a spectral method we further split it into linear (left side) and non-linear (right side) parts:

$$\frac{\partial\vec{A}}{\partial t} + s\vec{\nabla}\times(\vec{\nabla}\times\vec{A}) = -\chi(r)\vec{\nabla}\times(\vec{\nabla}\times\vec{A}) + {\rm Am}\frac{x_{\rm n}^2\tau_{\rm pn}}{n_{\rm c}}\left[\left\{\vec{\nabla}\times(\vec{\nabla}\times\vec{A})\right\}\times(\vec{\nabla}\times\vec{A}) - {\rm K}n_{\rm c}\vec{\nabla}(\Delta\mu)\right]\times(\vec{\nabla}\times\vec{A}), \tag{30}$$

where s is a constant dimensionless conductivity chosen at level 5×10^{-3}. This level is well below the conductivity of the crust but still above the conductivity of the core for temperature $T_9 = 0.2$. We show the comparison of these conductivities in Fig. 2 (right-hand panel). For the conductivity of the crust, we limit it at a value which corresponds to an Ohmic decay timescale of $t_{\rm crust} = 3\times10^7$ yr, using lower limit following the analysis by Igoshev (2019):

$$\sigma_{\rm crust} = \frac{c^2 t_{\rm crust}}{4\pi R_{\rm NS}}. \tag{31}$$

In the same Fig. 2, we show the radial profile of the coefficient $x_{\rm n}^2\tau_{\rm pn}/n_{\rm c}$ which determines the variation of the ambipolar diffusion speed over the NS core.

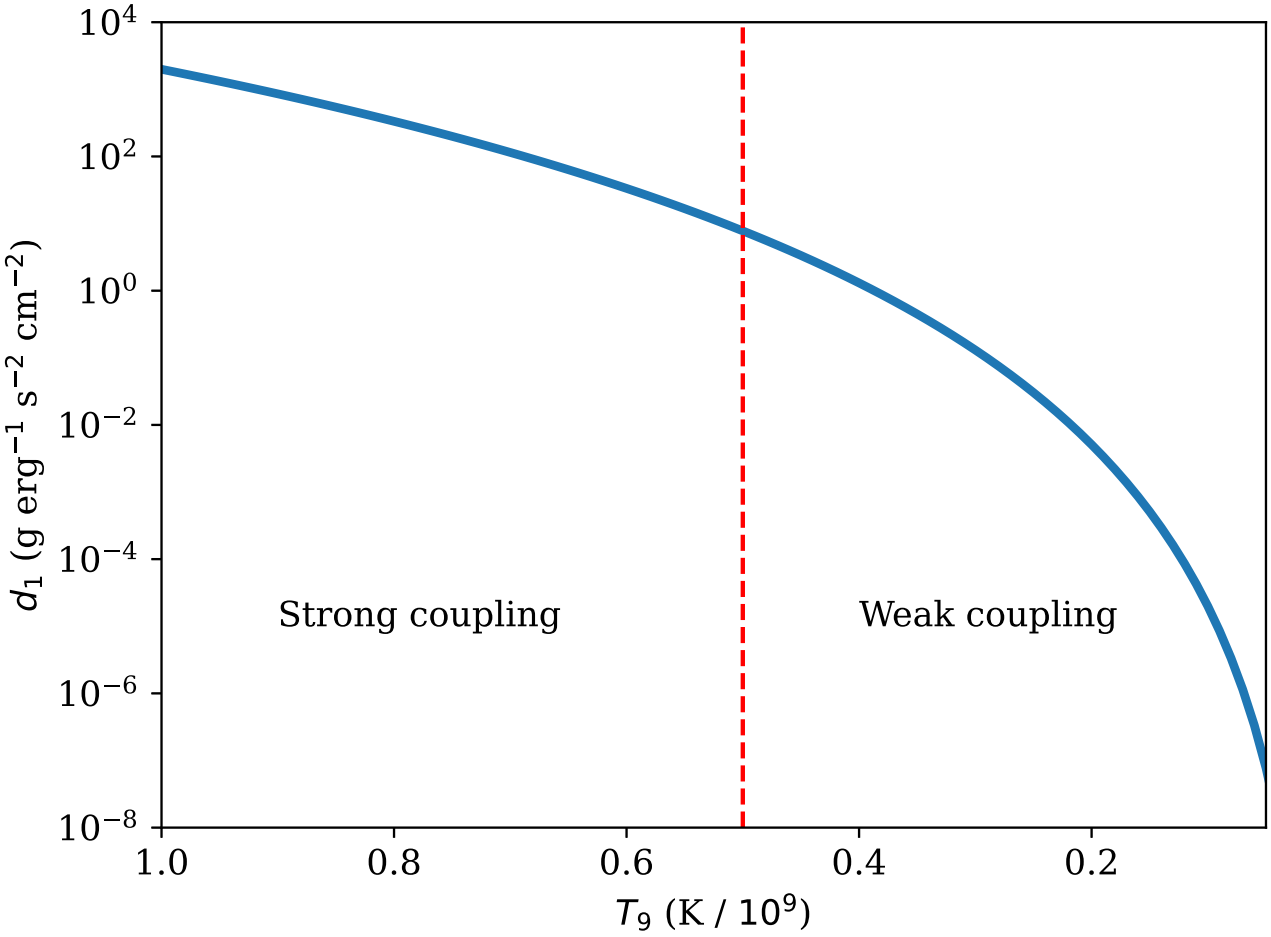

Figure 3. Dependence of d_1 on NS core temperature. The temperature axis is reversed to highlight the fact that NS cools down with time and thus moves from left to right.

In the second equation, we make the following replacements:

$$\vec{\nabla}^2(\Delta\mu) - d_1\xi_1(r)\Delta\mu = \frac{1}{K}\vec{\nabla}\cdot\left(\frac{(\vec{\nabla}\times(\vec{\nabla}\times\vec{A}))\times(\vec{\nabla}\times\vec{A})}{n_c}\right) - \frac{1}{K}\xi_3(r)((\vec{\nabla}\times(\vec{\nabla}\times\vec{A}))\times(\vec{\nabla}\times\vec{A}))\cdot\hat{r} + \xi_4(r)\frac{\partial\Delta\mu}{\partial r}. \tag{32}$$

The numerical coefficient d_1 is necessary to make the equation dimensionless, while $\xi_1(r)$, $\xi_3(r)$, and $\xi_4(r)$ are radial profiles within the NS core. The coefficient d_1 is computed as the following:

$$d_1 = \frac{m_{\rm p}^*\lambda_0 R_{\rm NS}^2}{n_{\rm c}^0\tau_{\rm pn}^0}. \tag{33}$$

We show the dependence of d_1 on core temperature in Fig. 3. The radial profiles are given as

$$\xi_1 = \frac{\lambda}{x_{\rm n}^2 n_{\rm c}\tau_{\rm pn}}, \tag{34}$$

$$\xi_3 = x_{\rm n}\tau_{\rm pn}\frac{\partial}{\partial r}\left(\frac{1}{x_{\rm n}\tau_{\rm pn}n_{\rm c}}\right), \tag{35}$$

$$\xi_4 = x_{\rm n}\tau_{\rm pn}n_{\rm c}\frac{\partial}{\partial r}\left(\frac{1}{x_{\rm n}\tau_{\rm pn}n_{\rm c}}\right). \tag{36}$$

In this second equation, we assumed that $x_{\rm n}\tau_{\rm pn}n_{\rm c}$ varies only along the radial direction.

In comparison to work by Passamonti et al. (2017) our coefficients translate to theirs as

$$a = \frac{R_{\rm NS}}{\sqrt{d_1\xi_1}}, \tag{37}$$

$$b = \frac{R_{\rm NS}}{\xi_4}. \tag{38}$$

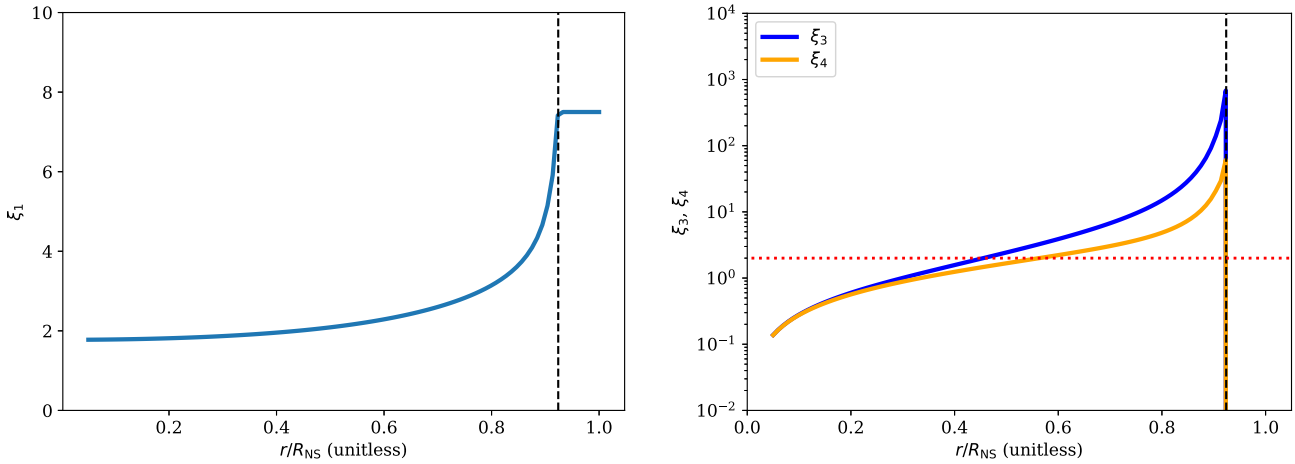

Figure 4. Profile of numerical coefficients ξ_1 (left-hand panel) and ξ_3, ξ_4 (right-hand panel). In the right-hand panel, we show the physical ξ_3, ξ_4 (solid blue and orange lines) and the value $r_{\rm cut} = 2$ at which we restrict our numerical profiles (horizontal red dotted line). Vertical dashed black line shows the crust–core boundary.

We show the radial profile for coefficients ξ_1, ξ_3, and ξ_4 in Fig. 4. We set the values of the ξ_3 and ξ_4 coefficients in the crust to be zero. It is not essential if $\Delta\mu \neq 0$ in the crust because we set the value of $n_{\rm c}$ (see Fig. 1) to zero in the crust, so ambipolar diffusion does not proceed there. The values of ξ_3 and ξ_4 change over a few orders of magnitude in the core. To avoid numerical difficulties for these realistic values of ξ_3 and ξ_4, we introduce a parameter $r_{\rm cut}$ which determines the maximum value which ξ_3 and ξ_4 can reach within the core. We provide more details about this $r_{\rm cut}$ parameter in Appendix B.

2.5 Strong and weak couplings

Because the value of d_1 is very sensitive to the NS core temperature, the behaviour of equation (32) changes when the NS cools down. Two different asymptotic cases are called strong coupling ($T_9 \sim 1$ and $d_1 \gg 1/K$) and weak coupling ($T_9 \sim 0$ and $d_1 \approx 1/K$).

In the strong coupling regime ($T > 5 \times 10^8$ K) the equation (32) transforms into:

$$\Delta\mu \approx 0.0, \tag{39}$$

because all coefficients in the original equation are dwarfed in comparison to $d_1 \approx 10^3$. Therefore, the material is in β-equilibrium. Alternatively, in a weak coupling regime the coefficient d_1 becomes comparable or smaller than the remaining terms in this equation.

2.6 Complete system of equations and boundary conditions

Overall, our system of equations includes also the Coulomb gauge $\nabla \cdot \vec{A} = 0$:

$$\frac{\partial \vec{A}}{\partial t} - s\nabla^2\vec{A} + \vec{\nabla}\Phi = \chi(r)\nabla^2\vec{A} + {\rm Am}\frac{x_{\rm n}^2\tau_{\rm pn}}{n_{\rm c}}\left[\left\{\vec{\nabla}\times(\vec{\nabla}\times\vec{A})\right\}\times(\vec{\nabla}\times\vec{A}) - {\rm K}n_{\rm c}\vec{\nabla}(\Delta\mu)\right]\times(\vec{\nabla}\times\vec{A}), \tag{40}$$

$$\vec{\nabla}\cdot\vec{A} = 0, \tag{41}$$

$$\vec{\nabla}^2(\Delta\mu) - \xi_4(r)\frac{\partial\Delta\mu}{\partial r} - d_1\xi_1(r)\Delta\mu = \frac{1}{K}\vec{\nabla}\cdot\left(\frac{(\vec{\nabla}\times(\vec{\nabla}\times\vec{A}))\times(\vec{\nabla}\times\vec{A})}{n_c}\right) - \frac{1}{K}\xi_3(r)((\vec{\nabla}\times(\vec{\nabla}\times\vec{A}))\times(\vec{\nabla}\times\vec{A}))\cdot\hat{r}, \tag{42}$$

where Φ is the scalar potential.

The vector potential $\vec{A}$ is subject to the potential boundary condition:

$$\frac{\partial\vec{A}_l}{\partial r} + \frac{l+1}{r}\vec{A}_l\Big|_{r=R_{\rm core}} = 0, \tag{43}$$

where l is the spherical harmonic degree. For the deviation from the β-equilibrium we use the same boundary condition as Passamonti et al. (2017):

$$Kn_{\rm c}\frac{\partial\Delta\mu}{\partial r} = \left(\vec{\nabla}\times(\vec{\nabla}\times A)\right)\times(\vec{\nabla}\times A)\cdot\hat{r}\Big|_{r=R_{\rm core}}. \tag{44}$$

This boundary condition means that $v_{\rm amb} = 0$ at the crust–core boundary, see equation (24).

Table 2. Summary of the setup for numerical simulations. $L_{\max}$ and $M_{\max}$ indicate the maximum spherical harmonic degree and order; $N_{\max}$ denotes the number of Jacobi polynomials in the radial direction.

Name	$L_{\max}$	$M_{\max}$	$N_{\max}$	Δt
A	32	64	24	2×10^{-5}
B	64	128	64	10^{-6}
C	64	128	128	2×10^{-7}
D	256	512	128	2×10^{-7}

2.6.1 Solution procedure

We solved the coupled partial differential equations (40)–(42) using the publicly available spectral code `Dedalus` v.3 (Lecoanet et al. 2019; Vasil et al. 2019; Burns et al. 2020) in spherical coordinates. This code expands the solution using a combination of spherical harmonics for angular directions and Jacobi polynomials for the radial direction. We propagate the simulation in time using the second-order implicit–explicit Runge–Kutta integrator (Ascher, Ruuth & Spiteri 1997). We rewrite the system of differential equations (40)–(42) to satisfy requirements of the `Dedalus` code as the following:

$$\frac{\partial \vec{A}}{\partial t} - s\nabla^2\vec{A} + \vec{\nabla}\Phi + \tau P(A) = \chi(r)\nabla^2\vec{A} + \mathrm{Am}\frac{x_n^2\tau_{pn}}{n_c}\left[\left\{\vec{\nabla}\times(\vec{\nabla}\times\vec{A})\right\}\times(\vec{\nabla}\times\vec{A}) - \mathrm{K}n_c\vec{\nabla}(\Delta\mu)\right]\times(\vec{\nabla}\times\vec{A}), \tag{45}$$

$$\vec{\nabla}\cdot\vec{A} + \tau_\phi = 0, \tag{46}$$

$$\vec{\nabla}^2(\Delta\mu) - \xi_4(r)\frac{\partial\Delta\mu}{\partial r} - d_1\xi_1(r)\Delta\mu + \tau P(\Delta\mu) + \tau_\mu = \frac{1}{K}\vec{\nabla}\cdot\left(\frac{(\vec{\nabla}\times(\vec{\nabla}\times\vec{A}))\times(\vec{\nabla}\times\vec{A})}{n_c}\right) - \frac{1}{K}\xi_3(r)((\vec{\nabla}\times(\vec{\nabla}\times\vec{A}))\times(\vec{\nabla}\times\vec{A}))\cdot\hat{r}. \tag{47}$$

We introduced so-called tau-terms: $\tau P(A)$ and $\tau P(\Delta\mu)$ in order to apply the generalized tau-method. These terms allow additional degrees of freedom, so the problem can be solved exactly over polynomials when the boundary conditions are introduced as additional equations in the system. There are two terms τ_ϕ and τ_μ which are the same at every point in the grid. These are introduced to deal with uncertainty of the type $A' = A + C$ where C is a constant. This uncertainty appears also for $\Delta\mu$ when d_1 is very small i.e. in the weak-coupling case. Because we introduced these two additional degrees of freedom not covered by the current set of equations and boundary conditions we add two more equations:

$$\int \Phi\, dV = 0, \tag{48}$$

$$\int \Delta\mu \mathrm{d}V = 0. \tag{49}$$

We store the results of simulations after every few thousand time-steps.

We run 3D simulations using spherical harmonics with different resolutions. We summarize the resolutions in Table 2. The lowest resolution is mostly used for testing purposes. The radial resolution is not uniform and grows toward the surface. In the setup B, the crust is covered with 15 collocation points in radial direction while the distance between consecutive collocation points near the NS centre is $0.024\, R_{\rm NS}$. The centre itself is not included as one of the radial grid points, since the coordinate singularity there would require it to be treated somewhat differently. The equatorial and meridional sections presented below therefore have a small empty circle at the centre. Depending on the strength of the magnetic field and the numerical resolution, the time-step is adjusted to ensure stability.

2.7 Initial conditions

For the initial magnetic field configuration we transform the analytical configuration by Akgün et al. (2013) to vector potential form:

$$\begin{aligned} A_r &= b_t, \\ A_\theta &= 0, \\ A_\phi &= \tfrac{f(r)}{r}\sin\theta, \end{aligned} \tag{50}$$

where

$$f(x) = \frac{35}{8}x^2 - \frac{21}{4}x^4 + \frac{15}{8}x^6. \tag{51}$$

The exact form of b_t together with derivations can be found in Appendix C. We add a Gaussian noise with amplitude of 10^{-5} to all components of $\vec{A}$. We are then in a position to study the stability of axisymmetric configurations to non-axisymmetric disturbances.

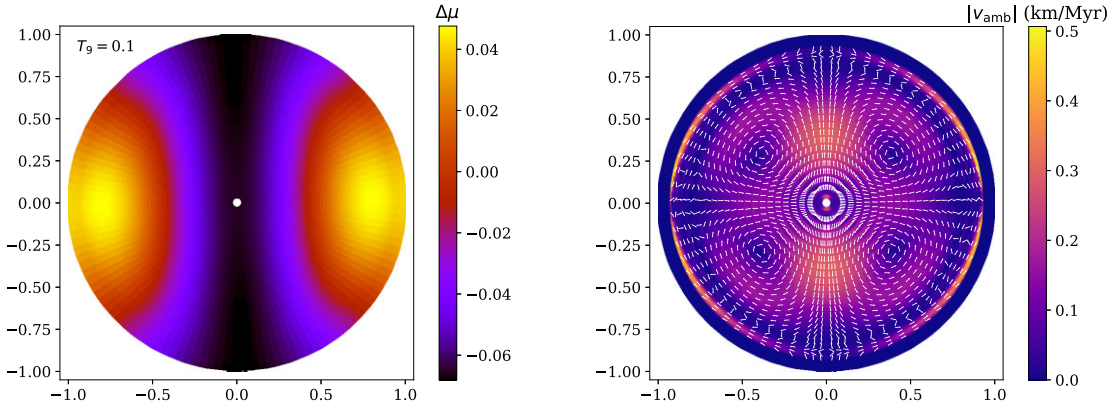

Figure 5. Left-hand panel: deviation from the chemical equilibrium. Right-hand panel: speed of ambipolar diffusion. These values are computed at the beginning of the simulation for $T_9 = 0.1$.

3 RESULTS

In order to check if our code works correctly we compute the deviation from the chemical equilibrium and the speed of ambipolar diffusion for a range of temperatures studied by Passamonti et al. (2017). We show the results of a short simulation with $T_9 = 0.1$ in Fig. 5. The velocity field is purely solenoidal. Our equation for the deviation from chemical equilibrium guarantees that the system relaxed to the magneto-hydrostatic quasi-equilibrium state at every time-step.

We make a few more verification runs. The goal of these runs is to check if the code correctly reproduces the previous results found in 2D simulations by Passamonti et al. (2017) and if our resolution is adequate to follow the long-term evolution of magnetic field. More details can be found in Appendix B. The main conclusions of these technical investigations are as follows: (1) we reproduce the results of Passamonti et al. (2017) with the exception of precise $\Delta\mu$ amplitudes, (2) our numerical resolutions presented in Table 2 are enough to resolve physics with $r_{\rm cut} = 2$, and (3) the exact choice of parameter $r_{\rm cut}$ does not seem to affect the development of the azimuthal field. It is worth noting important differences between our work and Passamonti et al. (2017): (1) our model includes the crust with finite conductivity, thus boundary conditions for magnetic field are written at the top of crust and not at the crust–core interface as was done by previous authors, (2) in our work we propagate the evolution of magnetic field in time while Passamonti et al. (2017) only solved for $\Delta\mu$ for different fixed temperatures.

We present our results in the following order. We start with discussing the basic physical variables such as speed of ambipolar diffusion, magnetic energy, azimuthal magnetic field, and electric currents. At this stage, we identify a development of non-axisymmetric instability. We characterize properties of this instability in Section 3.2. Further, we summarize the astrophysical implications in Section 3.3. Our basic run is computed with resolution B for 40 Myr and is numerically expensive. To cover the long-term behaviour, we also run simulations with resolution A for 160 Myr.

3.1 Basic physical variables

In this section, we describe how basic quantities evolve. We compute the speed of ambipolar diffusion using equation (24). In order to be more quantitative while characterizing the evolution of ambipolar velocity we introduce the mean ambipolar speed $\langle v_{\rm amb}\rangle$.

3.1.1 Speed of ambipolar diffusion

We plot the ambipolar diffusion velocities for temperature $T_9 = 0.1$ in Fig. 5. The maximum velocities reached within the NS are $\approx$0.5 km Myr^{-1}. These velocities are a few times larger than the value we initially estimated in Table 1. The reason for this is a mismatch between our $B_0 = 10^{14}$ G in Table 1 and the maximum magnetic field reached within the NS core, which is $B_{\rm max} \approx 8 \times 10^{14}$ G. Since $v_{\rm amb}$ depends on magnetic field strength as B^2, our velocities could be $\approx$64 times faster. This motion is partially cancelled by deviation from the chemical equilibrium. That is why maximum velocities are not $\approx$6 km Myr^{-1} but much slower. It also means that the time-scale of ambipolar diffusion is $\approx$5 times shorter, i.e. $t_{\rm amb} \approx 17$ Myr, or $\approx$2 in dimensionless time.

Here, we introduce a mean speed of ambipolar diffusion as

$$\langle v_{\rm amb}\rangle = \frac{1}{V}\int |v_{\rm amb}| d^3V, \tag{52}$$

where $|v_{\rm amb}|$ is the amplitude of the velocity vector and V is the total NS volume including the crust. There is a small caveat related to this definition. The speed of ambipolar diffusion in the crust is zero; our mean is thus slightly less in comparison to that we would obtain if we only integrated over the NS core. The mean speed of ambipolar diffusion initially decays with time, see Fig. 6. This speed starts growing again after $\approx$10 Myr, which corresponds to development of an instability. The initial decrease of ambipolar velocity is related to the decay of magnetic

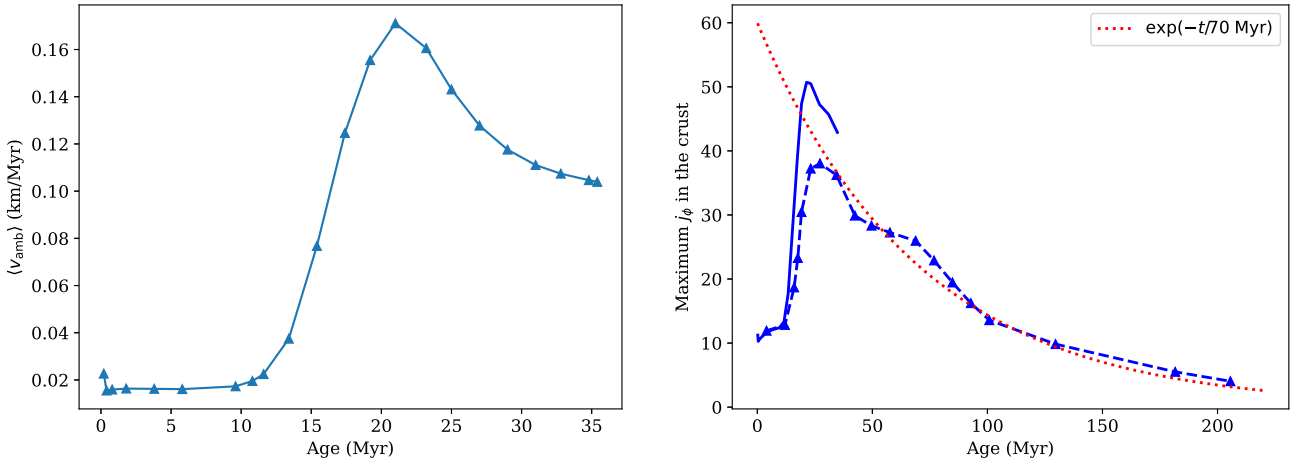

Figure 6. Left-hand panel: evolution of mean ambipolar velocity inside the neutron star. Right-hand panel: evolution of maximum azimuthal electric current in NS crust between radial distance of 0.924 R_{NS} and 0.955 R_{NS}. In both panels, we show simulations with $r_{cut} = 2$. Solid lines correspond to simulations with resolution B while dashed lines correspond to similar calculations with resolution A.

fields generated due to the noise added to the simulations. The mean speed reaches its maximum around 20 Myr, i.e. on the time-scale of ambipolar diffusion.

We show the extended evolution of ambipolar velocity in Fig. 7. Around dimensionless time 1, north–south symmetry is broken. The velocity field in the Northern hemisphere behaves differently than the velocity field in the Southern hemisphere. After dimensionless time 2, the axial symmetry is broken, i.e. the velocity field in the right part of the figure does not look the same as the velocity field in the left part of the same figure.

3.1.2 Magnetic energy

We compute the total magnetic energy in our simulations as

$$E_t = \frac{1}{2} \int \left(\vec{\nabla} \times \vec{A} \right)^2 \mathrm{d}^3 V. \tag{53}$$

It decays slowly during the simulations, see Fig. 8. In the shorter simulations the energy seems to decay nearly linearly with time. During the first 35 Myr half of the total magnetic energy is released from the system. This decay rate is surprising since the Ohmic decay time-scale in the core is chosen to be fixed at 6 Gyr. This decay time-scale is comparable with the time-scale of ambipolar diffusion (≈20 Myr) and the Ohmic time-scale in the crust (30 Myr). We can estimate the time-scale for energy decay in high-resolution simulations using the exponential model as

$$t_{\mathrm{decay}} = -\frac{t}{\log E_t(t) - \log E_t(0)} \approx 50 \text{ Myr}. \tag{54}$$

In our first attempt to model the non-axisymmetric evolution of magnetic fields, we add random values to all components of the initial vector potential $\vec{A}$ with amplitude of 10^{-5} in dimensionless units. We further check how these perturbations evolve, tracking the non-axisymmetric part of the total magnetic energy. In order to compute this quantity, we compute first the axisymmetric part of the magnetic energy by averaging the field over the ϕ-coordinate:

$$\vec{B}_{\mathrm{axi}} = \frac{1}{2\pi} \int_0^{2\pi} \vec{B}(r, \theta, \phi) \mathrm{d}\phi. \tag{55}$$

Then we find the energy as

$$E_{\mathrm{axi}} = \pi \int \vec{B}_{\mathrm{axi}}^2 \mathrm{d}^2 V. \tag{56}$$

The non-axisymmetric part of magnetic energy is then:

$$E_{\mathrm{non}} = E_t - E_{\mathrm{axi}}. \tag{57}$$

We plot the evolution of E_{non} in Fig. 8. We notice that until $t = 2$ Myr it decays much faster than the total magnetic energy, so initially the field becomes more axisymmetric. However, once the random initial conditions have adjusted themselves, after 2 Myr the non-axisymmetric part of the energy grows, reaching values of 0.3, several orders of magnitude greater than the initial perturbations. That is, the large-scale axisymmetric field is unstable to the presence of the small-scale non-axisymmetric noise that was added. The non-axisymmetric magnetic energy peaks around time 2.7, and thereafter decays slower than the total magnetic energy. This means that the instability continues to operate, and a fraction of non-axisymmetric energy is constantly regenerated from the large-scale axisymmetric field.

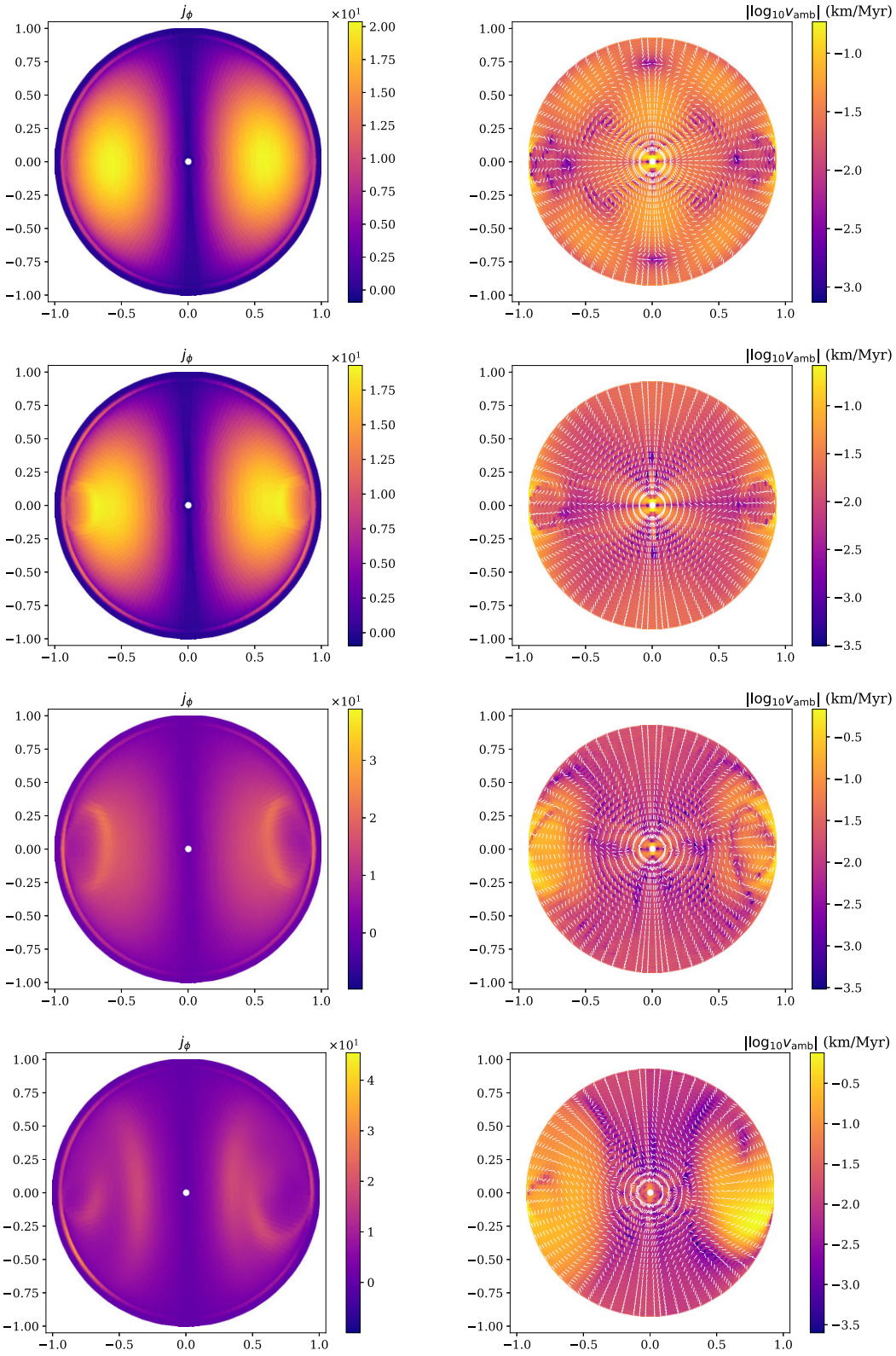

Figure 7. The left column shows the electric current j_ϕ, and the right column the speed of ambipolar diffusion v_{amb}, computed for resolution B and $r_{cut} = 2$. From top to bottom the four rows are at times $t = 0.02$, 0.96, 1.73, and 3.14.

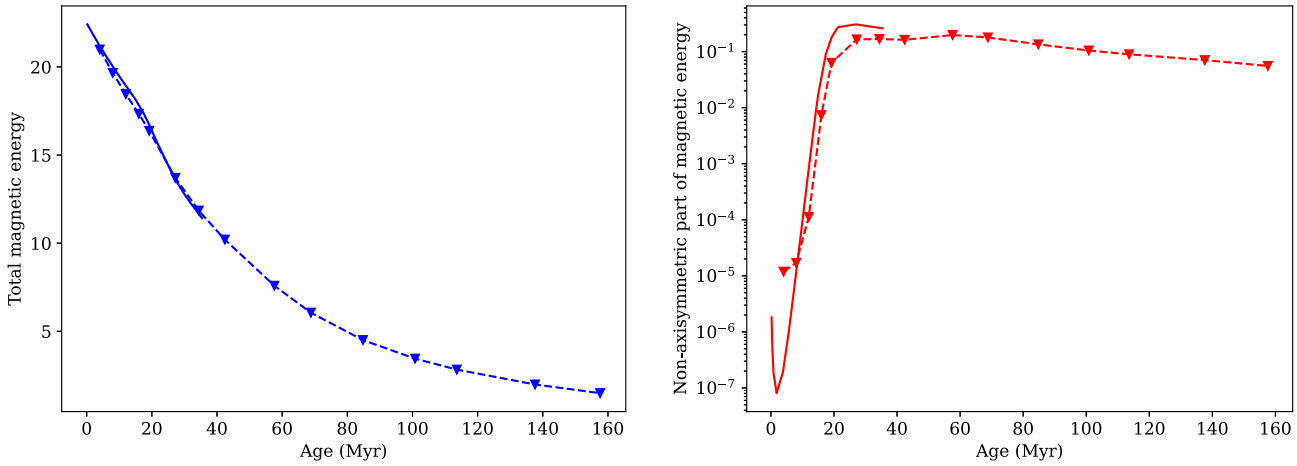

Figure 8. Left-hand panel: evolution of total magnetic energy E_t. Right-hand panel: evolution of non-axisymmetric part E_n. On both panels, we show simulations with $r_{\rm cut} = 2$. Solid lines correspond to simulations with resolution B while dashed lines correspond to similar calculations with resolution A.

3.1.3 Azimuthal magnetic field

The evolution of the non-axisymmetric part of the energy is easy to track if we examine the B_ϕ component of the field, which roughly corresponds to toroidal magnetic field because our initial conditions are nearly axisymmetric, see Fig. 9. In our initial conditions, we have very limited B_ϕ caused by the random perturbations of A_r and A_θ because we assume regular magnetic field only for A_ϕ. During the simulations these perturbations merge, forming complicated semiregular large-scale structures inside the NS core. Initially, these structures are elongated along the magnetic field lines with width 300–600 m and length comparable to $R_{\rm NS}$.

Over time these elongated structures decay and merge, forming much larger regions with regular B_ϕ. After a few million years the strength of magnetic fields in these structures starts growing, reaching values of 3×10^{12} G. When we examine the equatorial cut we observe that B_ϕ reaches positive and negative values 14 times, that is, the azimuthal wavenumber $m = 14$. This is well within our numerical resolution (recall Table 2), so we believe that these structures correspond to true physical instabilities rather than numerical ones. We further test issues related to resolution and the influence of $r_{\rm cut}$ in Appendix B.

The long calculations (above 35 Myr) with resolution B are numerically challenging. Nevertheless, we are still interested in later stages of this simulations, so we revert back to resolution A for extended calculations. We show some results of these calculations in Fig. 10. In these simulations the structure of magnetic field stays quite similar to more detailed simulations; compare the last panel of Fig. 9 with the first panel of Fig. 10. On longer time-scales the fine structures of B_ϕ continue merging so by 100 Myr the $m = 4$ mode becomes dominant.

3.1.4 Electric currents

Among other quantities we track the evolution of electric current. In our simulation setup electric currents in the crust are expected to decay on a 30 Myr time-scale. Soon after we start the simulations, we see the formation of electric current near the core-crust boundary, see Fig. 7. In our simulations this current is localized between the crust–core boundary ($0.924R_{\rm NS}$) and radial distance $\approx 0.955R_{\rm NS}$ in the region where the resistivity grows rapidly (see Fig. 2). In this region, resistivity still does not reach its maximum. Some electric current also flows through the outer crust where the resistivity is fixed. We resolve the current above the crust-core boundary relatively well since this region is covered with 4 collocation points in numerical simulations with resolution B and with 8 collocation points in simulations with resolution D. In both these simulations the radial extent of the current is the same, confirming that this current sheet is adequately resolved.

Under the influence of ambipolar diffusion the electric currents in the core start evolving, forming arcs reaching from the core–crust boundary to distances $R = 0.3$–$0.5\ R_{\rm NS}$ inside the NS, see Fig. 7. The electric current in the crust evolves as well, see Fig. 6. In this figure, we show the time evolution of maximum j_ϕ between radial distance $0.924\ R_{\rm NS}$ and $0.955\ R_{\rm NS}$. Ambipolar diffusion induces strong electric current in the NS crust after 15 Myr. The current reaches a maximum around 20 Myr and decays nearly exponentially after this. This current decays on approximately twice the Ohmic time-scale (60–70 Myr) of the crust, leading to global decay of magnetic energy on a time-scale comparable to the Ohmic time-scale in the crust. At later stages ($t > 1.5$) most of the crust current concentrates between $\pi/4 < \theta < 3\pi/4$, see Fig. 7. At advanced stages of evolution the arcs of electric current separate regions with fast ambipolar diffusion speed ($v_{\rm amb} > 0.1$ km Myr^{-1}) from regions with slow ambipolar diffusion speed.

3.2 Instability of poloidal magnetic field

As we noted in previous sections the non-axisymmetric part of total magnetic energy begins growth at 2–3 Myr and reaches maximum around 21 Myr, see Fig. 8. Simultaneously, the speed of ambipolar diffusion starts growing and reaches maximum around the same time. We also

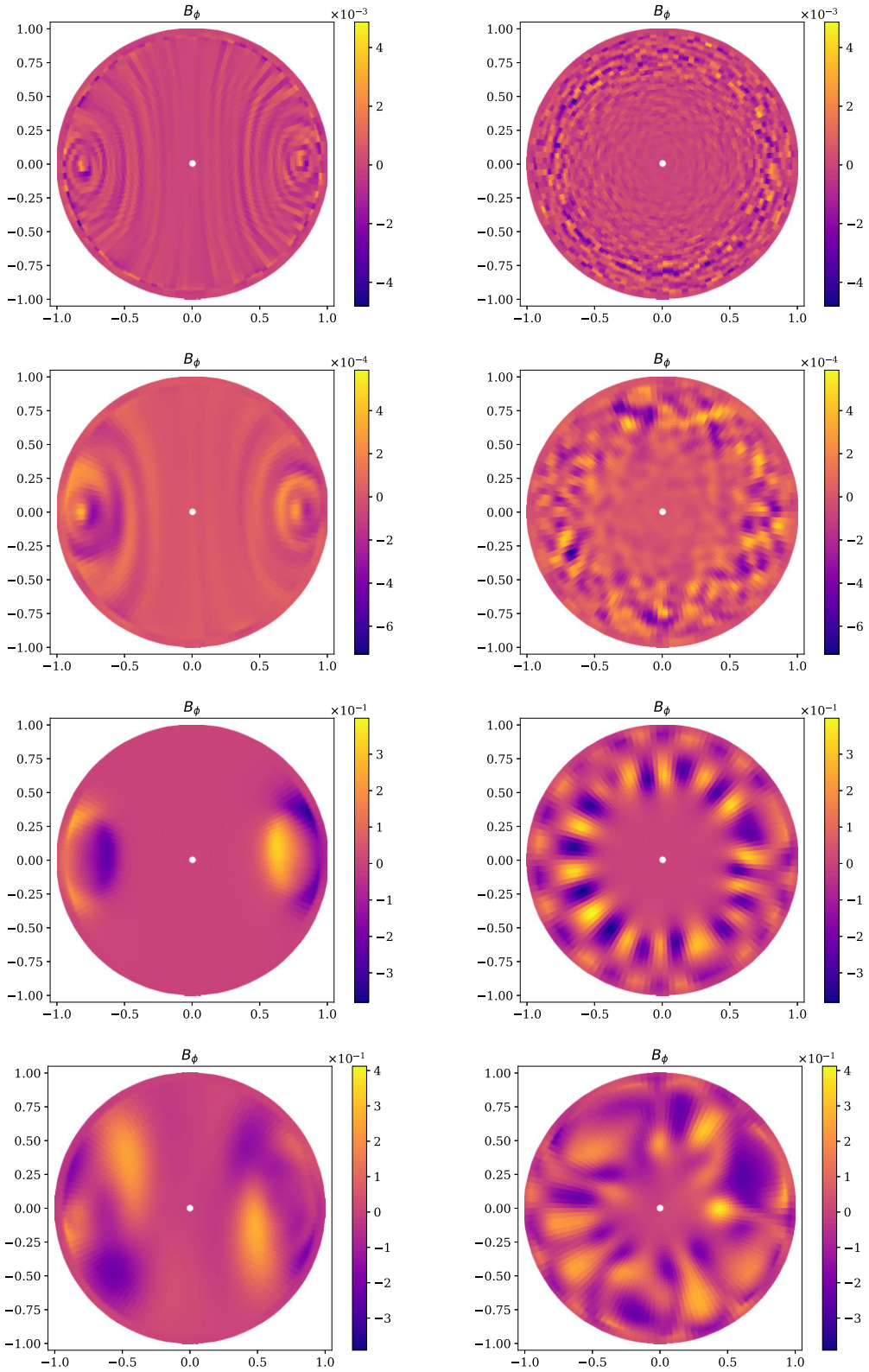

Figure 9. Evolution of B_ϕ with time. The left column shows meridional cuts through the NS while the right column shows equatorial cuts. The resolution is B, and $r_{\rm cut} = 2$. From top to bottom the four rows are $t = 0.02$, 0.18, 1.74, and 3.54.

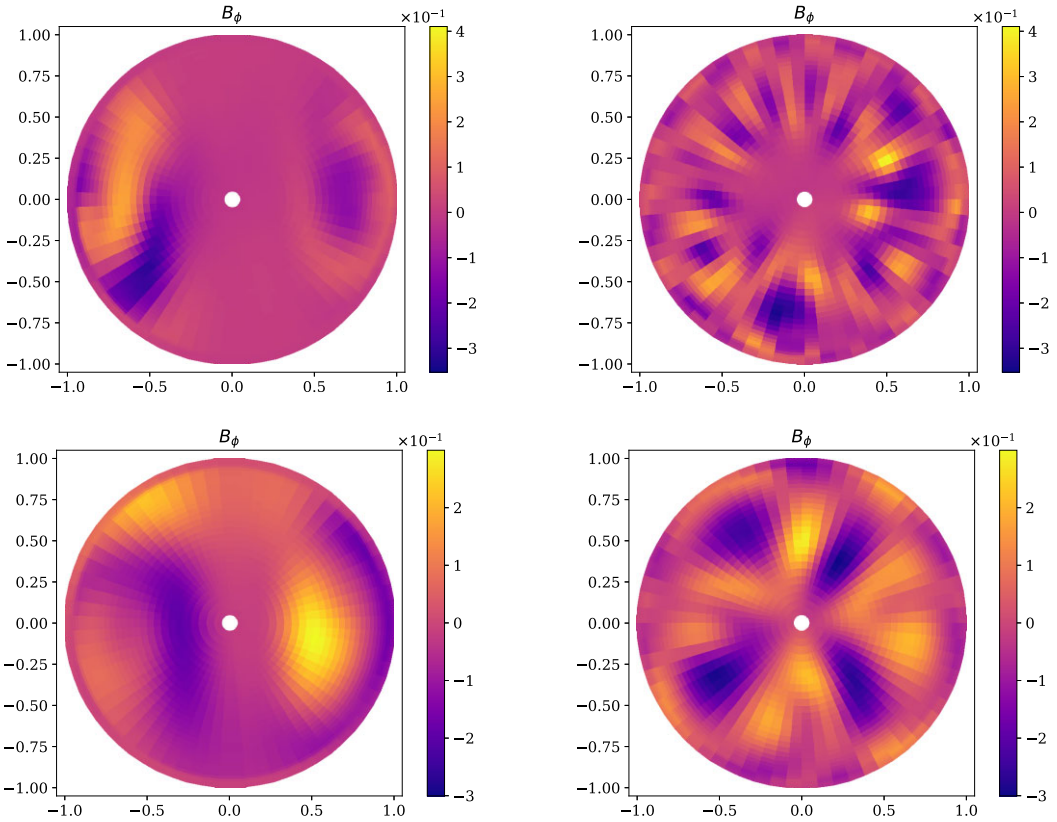

Figure 10. Evolution of B_ϕ with time. The left column shows meridional cuts through the NS while the right column shows equatorial cuts. The resolution is A, and $r_{\rm cut} = 2$. The top row is $t = 3.52$ and the bottom row $t = 10.08$.

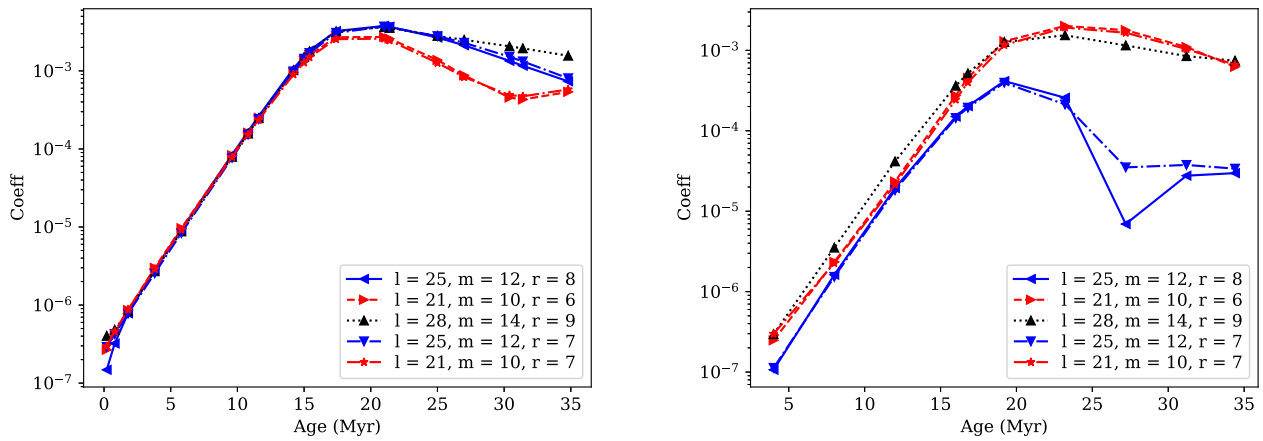

Figure 11. Growth of selected coefficients of the magnetic field with time; l, m correspond to spherical harmonic degree and order, while r corresponds to degree of Jacobi polynomial. In the left-hand panel, we show the result of calculations with resolution B and in the right-hand panel we show the truncated results computed with resolution A.

noted that azimuthal magnetic field with $m \approx 14$ start emerging from the initial fluctuations. The azimuthal number $m = 14$ is seen as the number of regions with negative values of B_ϕ in the equatorial cut in Fig. 9.

In order to investigate growth of azimuthal magnetic field in more detail, we identify the coefficients of the spectral expansion with the largest absolute value at age 15 Myr. From this selection we exclude the coefficients corresponding to the initial condition. We plot the evolution of this identified cluster of harmonics in Fig. 11 for numerical resolutions A and B. The contribution of these harmonics to the solution increases from 10^{-7} (roughly the level of noise perturbations added to the simulations) to $(2 - 3) \times 10^{-3}$ when these harmonics start affecting the ambipolar velocity field. Although the resolution A is only half of the resolution B, we see the growth of exactly the same harmonics during the first 15 Myr. The behaviour after the saturation is different, which means that after the saturation harmonics with number $l > 32$ start contributing to the evolution.

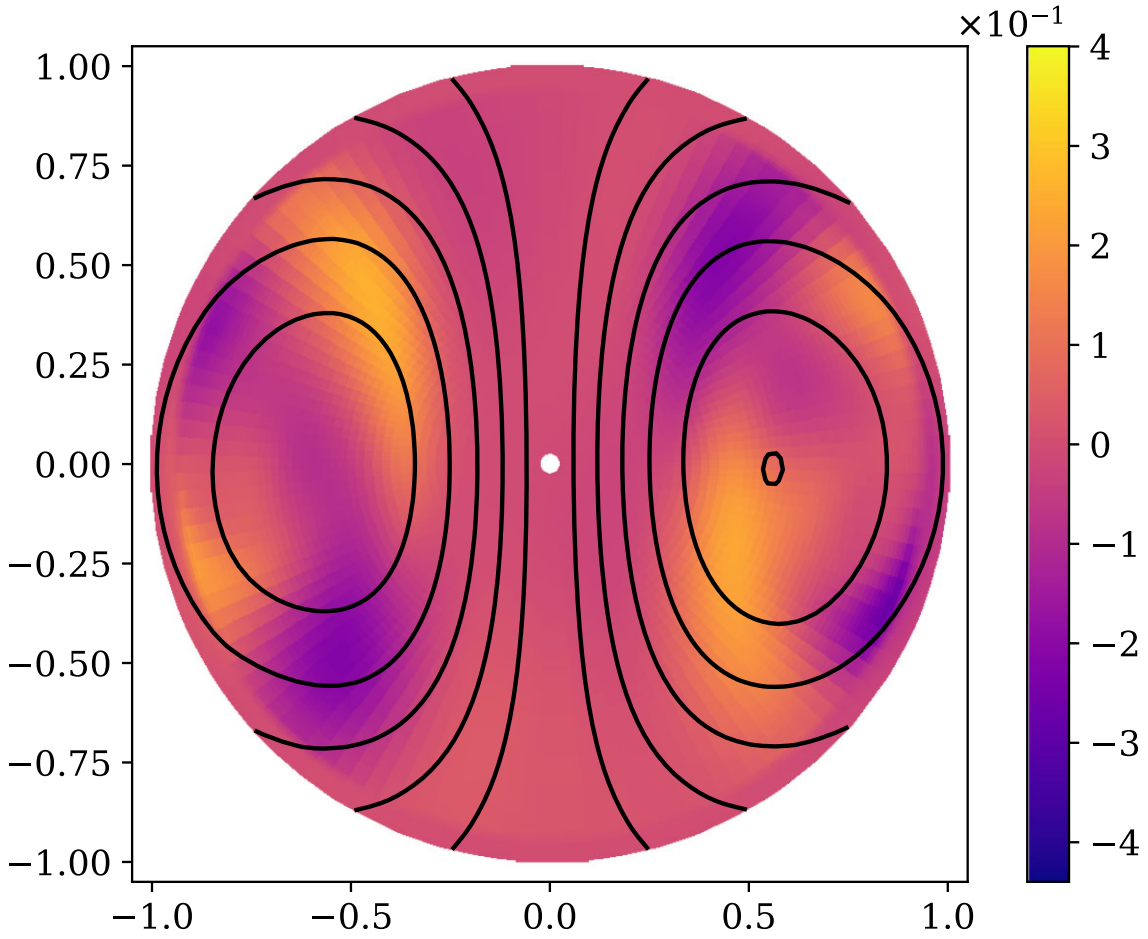

Figure 12. A meridional cut showing the B_ϕ component of magnetic field at 29 Myr, computed with resolution B. Colour shows the strength of B_ϕ while black solid lines correspond to field lines for B_r and B_θ components.

The growth of well-resolved spectrally localized structures is an indication of instability. We have thus shown that an initial axisymmetric poloidal magnetic field is unstable under effects of ambipolar diffusion in three dimensions, giving rise to non-axisymmetric structures. Using Fig. 11, we conclude that the growth rate of this instability is ≈2 Myr or 0.2 in dimensionless units. The instability is saturated around 15–20 Myr when the selected harmonics reach maximum value.

This instability is intrinsically 3D and was not seen before in 1D and 2D simulations. Earlier on, Castillo et al. (2017) found a formation of toroidal magnetic field in 2D, axisymmetric simulations. Our azimuthal field might be related to that one but has a complicated structure in the azimuthal direction. Castillo et al. (2017) found that their newly generated toroidal magnetic field is bounded within the closed magnetic field lines of poloidal magnetic field. It is not the case in our simulations. In Fig. 12, we see that B_ϕ is generated also in regions of open field lines. This difference might be related to the following factors: (1) our simulations are not axisymmetric, (2) our B_ϕ is therefore also not a purely toroidal magnetic field, and (3) we added a crust with finite conductivity in our simulations.

We show evolution of magnetic energy computed in our low-resolution simulations (A resolution) in Fig. 8. The total magnetic energy decay is quite similar to that computed in high-resolution simulations (B resolution). There are some small differences around 20 Myr which might be related to a slight delay in development of non-axisymmetric magnetic field. On longer time-scales it becomes apparent that magnetic energy decay is exponential with time-scale of ≈60 Myr, i.e. ≈3 ambipolar diffusion time-scales estimated using velocities derived from the numerical solution. The energy decays in our simulations much faster and much stronger than it was found in axisymmetric simulations by Castillo et al. (2017). We do not see any indications that magnetic energy stops decaying after some time. We could speculate that magnetic energy decay might slow down when total magnetic energy becomes comparable (i.e. 2–3 times stronger) to the non-axisymmetric part of the energy. It will require a decay of one order of magnitude more, i.e. on a time-scale of another 150 Myr.

3.3 Astrophysical implications

In this section, we summarize the results of our simulations which could be probed in astronomical observations. These are the structure and evolution of surface magnetic field, surface temperature, and crust failure.

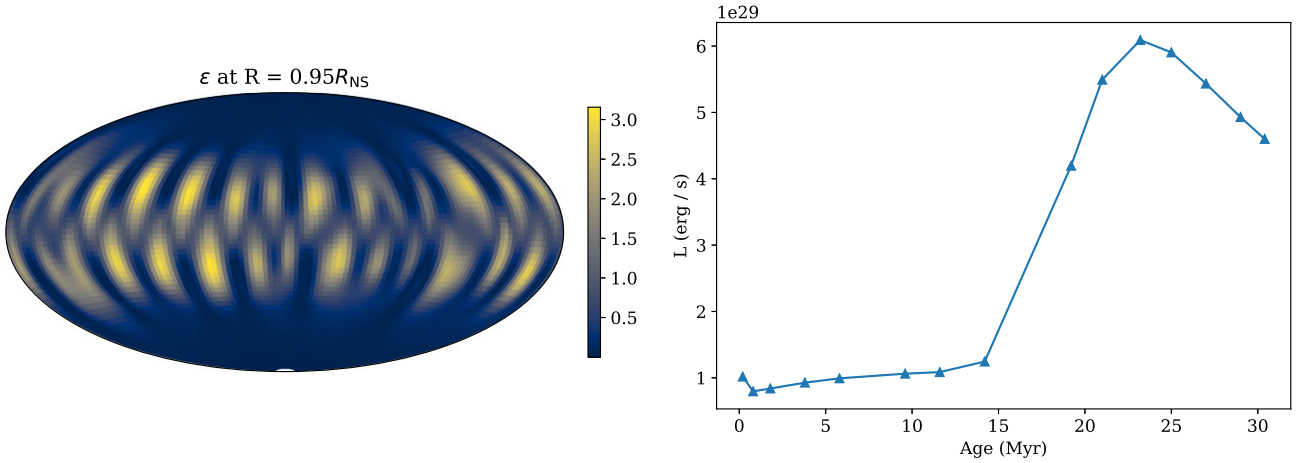

Figure 13. Left-hand panel: energy release in the NS crust rate due to the Ohmic decay at 23 Myr for $r_{\rm cut} = 2$ at depth $R = 0.95$ $R_{\rm NS}$. Right-hand panel: luminosity as a function of time.

3.3.1 Deep crustal heating

The presence of electric currents in the crust lead to its heating. We can estimate the rate of this heating as follows (see e.g. De Grandis et al. 2020, Igoshev et al. 2021a):

$$\epsilon = \frac{1}{\sigma}\left[\frac{c}{4\pi}(\vec{\nabla}\times\vec{B})\right]^2 \ \text{erg cm}^{-3}\ \text{s}^{-1}. \tag{58}$$

In our dimensionless system the energy release rate is:

$$\epsilon = \chi(r)\left[\vec{\nabla}\times(\vec{\nabla}\times\vec{A})\right]^2. \tag{59}$$

We show this dimensionless quantity in Fig. 13. Most of the energy is released in the deep NS crust around $R = 0.95$ $R_{\rm NS}$. To convert the dimensionless energy release into cgs units, we use the conversion factor:

$$\epsilon_0^v = \frac{c^2 B_0^2}{16\pi^2 R_{\rm NS}^2 \sigma_0}, \tag{60}$$

which is the volumetric energy release rate. Thus each cm^3 in the deep crust releases up to $\approx 10^{12}$ erg s^{-1}, see Table 1. If we numerically integrate this energy release over the whole NS we obtain:

$$\epsilon_t = \int \chi(r)\left[\vec{\nabla}\times(\vec{\nabla}\times\vec{A})\right]^2 \mathrm{d}V. \tag{61}$$

To convert this value into cgs we use the value:

$$\epsilon_0 = R_{\rm NS}^3 \epsilon_0^v. \tag{62}$$

We plot the evolution of the energy release rate in Fig. 13. During the first 10 Myr the energy release rate stays at the level of $\approx 10^{29}$ erg s^{-1}. Since energy is released in the deep crust, a part of this energy could be emitted as neutrino radiation and cannot be detected. If a significant fraction of this energy reaches the NS surface it allows the NS to stay relatively hot with surface temperature given by

$$T = \left(\frac{L}{4\pi R_{\rm NS}^2 \sigma_B}\right)^{1/4} \approx 10^5\ \text{K}. \tag{63}$$

The energy release starts growing after 1 Myr when the instability started developing. The heat release reaches its maximum around 20–25 Myr when the instability reaches its saturation.

Spatially, the energy release concentrates towards the magnetic equator where the crust thermal conductivity is limited. Further simulations of magneto-thermal evolution are required to understand what the surface map could look like. In any case the heat is not concentrated toward small-scale structures but instead forms a wide belt around the equator. This thermal emission might thus be detected as the bulk NS emission. It is known that some older NSs have bulk temperatures comparable to 10^5 K (see e.g. Mignani, Pavlov & Kargaltsev 2008; Pavlov et al. 2009).

The magnetic energy decays and this energy is released from the system in the form of the deep crust heating which evolves with age. The energy release pattern in the deep crust also has azimuthal angular structure with $m = 14$; that is, it is the same as the current structure. Thus, this pattern evolves with time and by 160 Myr simplifies to $m = 4$.

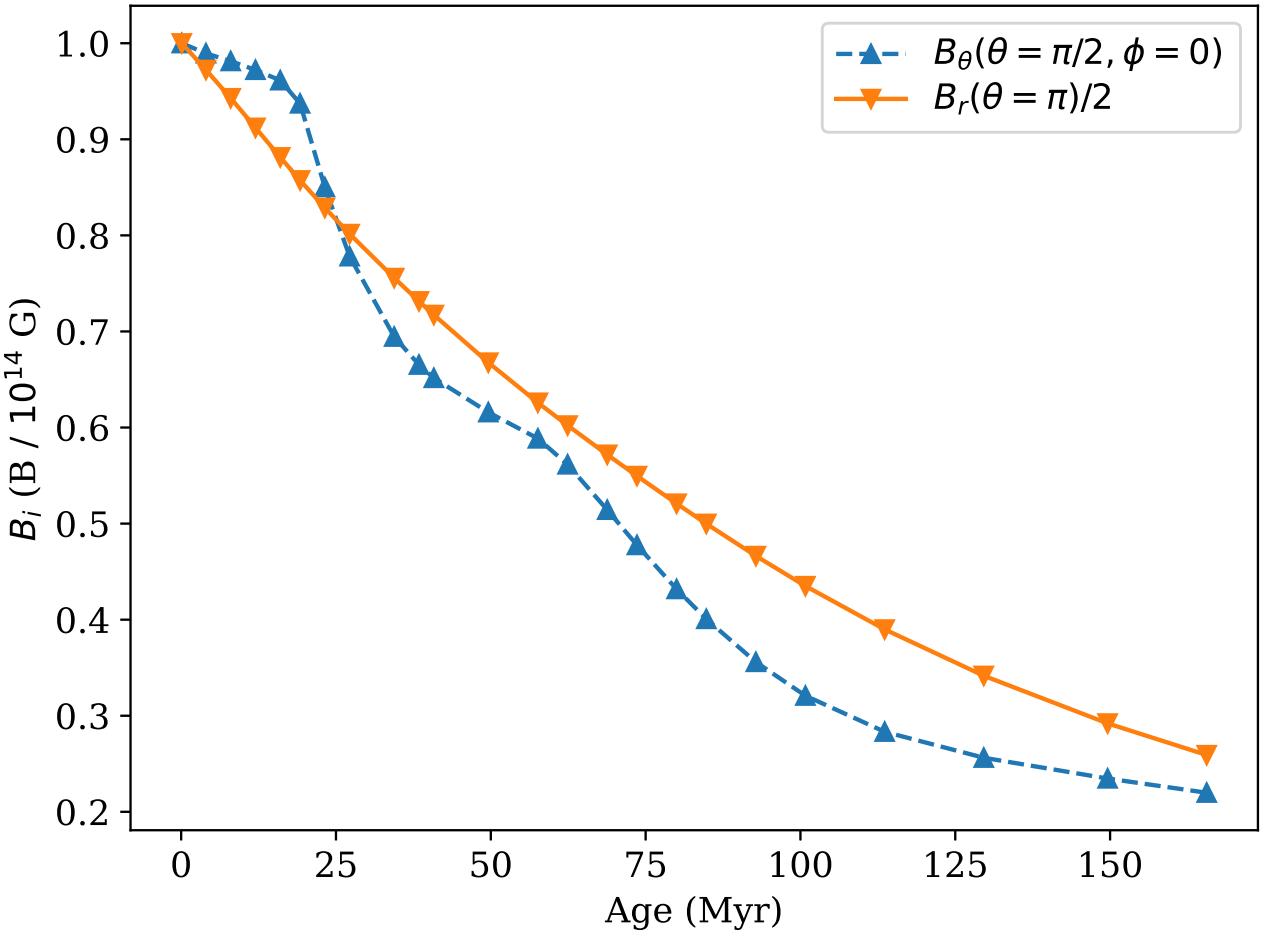

Figure 14. Evolution of surface magnetic field strength as a function of time.

3.3.2 *Structure and evolution of surface magnetic field*

We show the evolution of magnetic field strength at the equator and pole in Fig. 14. While the surface field at the pole decays with the same rate, the field at the equator is affected by the growth of the small-scale field. Its decay thus proceeds with different rates. Overall, the decay of magnetic field proceeds on a time-scale of ≈120 Myr, i.e. on twice the time-scale for decay of magnetic energy ($E \propto B^2$), and on the time-scale of six ambipolar diffusion time-scales estimated based on numerical velocity. We see no indications that magnetic field decay stops. It is possible to extrapolate that in our particular setup we could suggest that a magnetar-strength field decays to values of 10^8 G on a time-scale of 1.1 Gyr under the influence of ambipolar diffusion.

Small-scale magnetic field with $m = 14$ emerges to the NS surface on a time-scale of 2 Myr. This structure is most noticeable in the B_ϕ component, which was absent in our initial conditions. In Fig. 15 we show B_r and B_ϕ components of magnetic field. This component has filaments stretching in the north–south direction. The B_ϕ component has a clearer $m = 14$ structure. The surface pattern evolves and forms $m = 4$ by 160 Myr. As is clear from the plots, the dipolar component stays dominant even at these long time-scales, although the degree of dominance falls from 15 times to 4 times.

Unexpected small-scale magnetic fields were discovered in millisecond radio pulsars (see e.g. Bilous et al. 2019). Our results indicate that ambipolar diffusion could give rise to higher order multipoles in old neutron stars.

3.3.3 *Crust failure*

The electric current formed as a result of ambipolar diffusion could lead to crust failure. To check if it is the case we compute the elastic strain tensor $\hat{\sigma}$ following the prescription of (Lander et al. 2015; Gourgouliatos, De Grandis & Igoshev 2022):

$$\sqrt{\frac{1}{2}\sigma_{ij}\sigma^{ij}} = \frac{1}{8\pi\mu_{\rm shear}}\sqrt{B^2B_0^2 + \frac{3}{2}B^4 + \frac{3}{2}B_0^4 - 4(\vec{B}\cdot\vec{B}_0)^2}, \tag{64}$$

where we used the Einstein summation rule, and $\mu_{\rm shear}$ is the shear modulus of the NS crust, assumed to be 10^{30} dyn cm^{-2} (Ruderman 1969). More modern estimates for the shear modulus close to the core–crust boundary are 1.8×10^{30} dyn cm^{-2} (Hoffman & Heyl 2012). In equation (64), $\vec{B}_0$ stands for the initial magnetic field configuration when the crust froze. The magnetic field $\vec{B}$ is the instantaneous magnetic

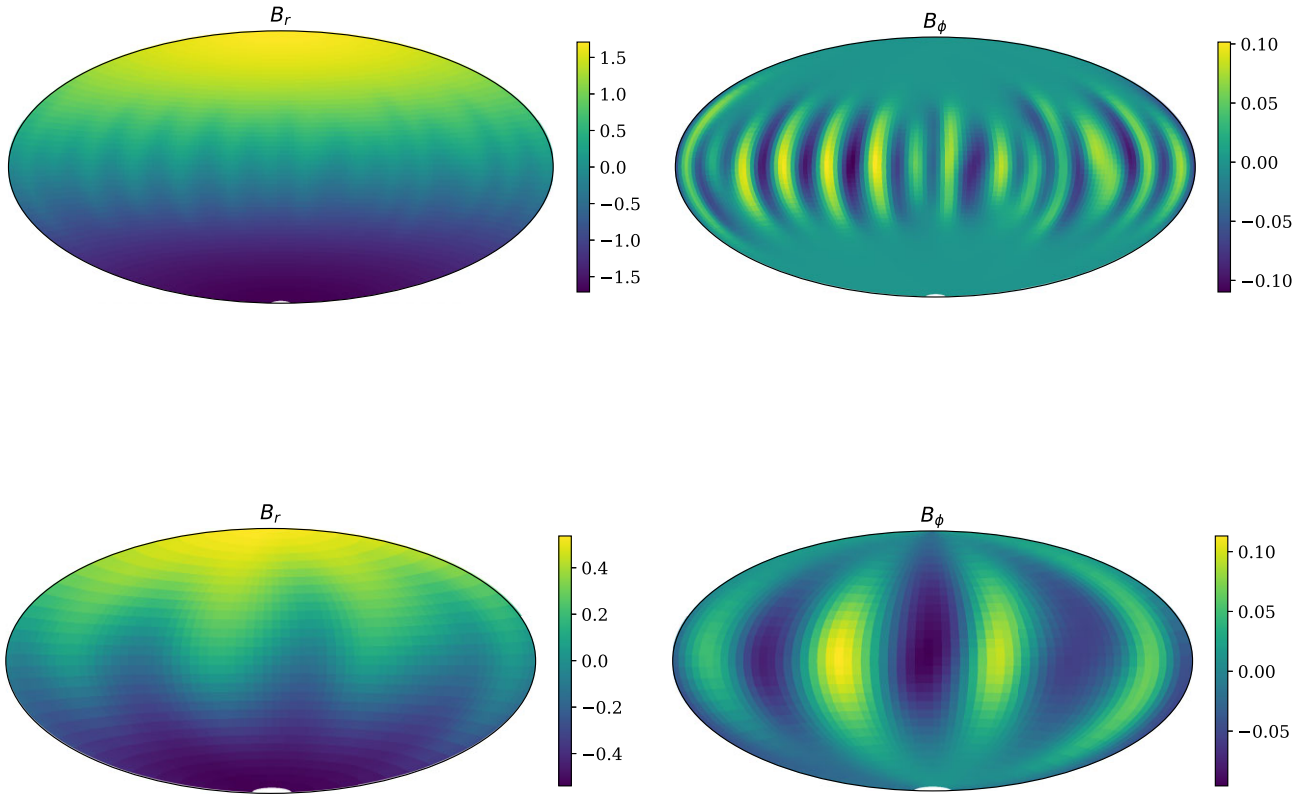

Figure 15. Surface magnetic field for $r_{\rm cut} = 2$ at dimensionless time 21 Myr (top row) and at 161 Myr (bottom row).

field. The NS crust fails according to the von Mises criterion (Mises 1913) when:

$$\sqrt{\frac{1}{2}\sigma_{ij}\sigma^{ij}} > 0.1, \tag{65}$$

where 0.1 is the maximum breaking strain. We plot the value of NS crust strain in Fig. 16. The maximum value after 15 Myr of evolution is 2.5×10^{-3} which is not enough to break the crust.

4 CONCLUSIONS

In this work, we used the `Dedalus` code to study ambipolar diffusion in neutron star cores. Unlike the previous analysis in one and two dimensions, we integrate the equations in three dimensions using the spherical coordinate system. We also include the neutron star crust with finite conductivity.

Our work has following caveats:

(i) A neutron star core is expected to be in a superconducting and superfluid state, which will probably significantly affect the magnetic field evolution described here. Despite the significant progress recently reached in investigations of how neutron vortices and magnetic flux tubes interact with each other, the detailed equations describing the evolution and its importance is a matter of active scientific debate. Therefore, we refrain from implementing the superfluidity and superconductivity at the moment.

(ii) We assume negligible baryon velocity, which is not the case at the beginning of the simulations. The main expected impact of this assumption is that we underestimated the speed of ambipolar diffusion, which might be a factor of a few times faster than in our simulations. Because of this assumption we are able to write equations in the one-fluid approximation. In future work we plan to implement the two-fluid approximation.

(iii) Given limitations in computing power we had to restrict radial profiles for coefficients ξ_3 and ξ_4 by introducing the parameter $r_{\rm cut} = 2$. Under realistic conditions we see the formation of a compact current sheet at the crust–core boundary in the equatorial plane with radial extent smaller than 50 m, which corresponds to our finest resolution.

Given these caveats, we discovered the instability of pure poloidal axisymmetric magnetic field under influence of ambipolar diffusion in weak coupling mode. This instability leads to development of wave-like B_ϕ (kind of toroidal component) which is composed of harmonics with $l = 21, 25, 28$ with $m = 10, 12, 14$. This well-resolved cluster of harmonics grows from initial perturbations by four orders of magnitude over the first 15 Myr (1.5 dimensionless times for $B_0 = 10^{14}$ G). The growth of instability is exponential with a typical time-scale of 2 Myr

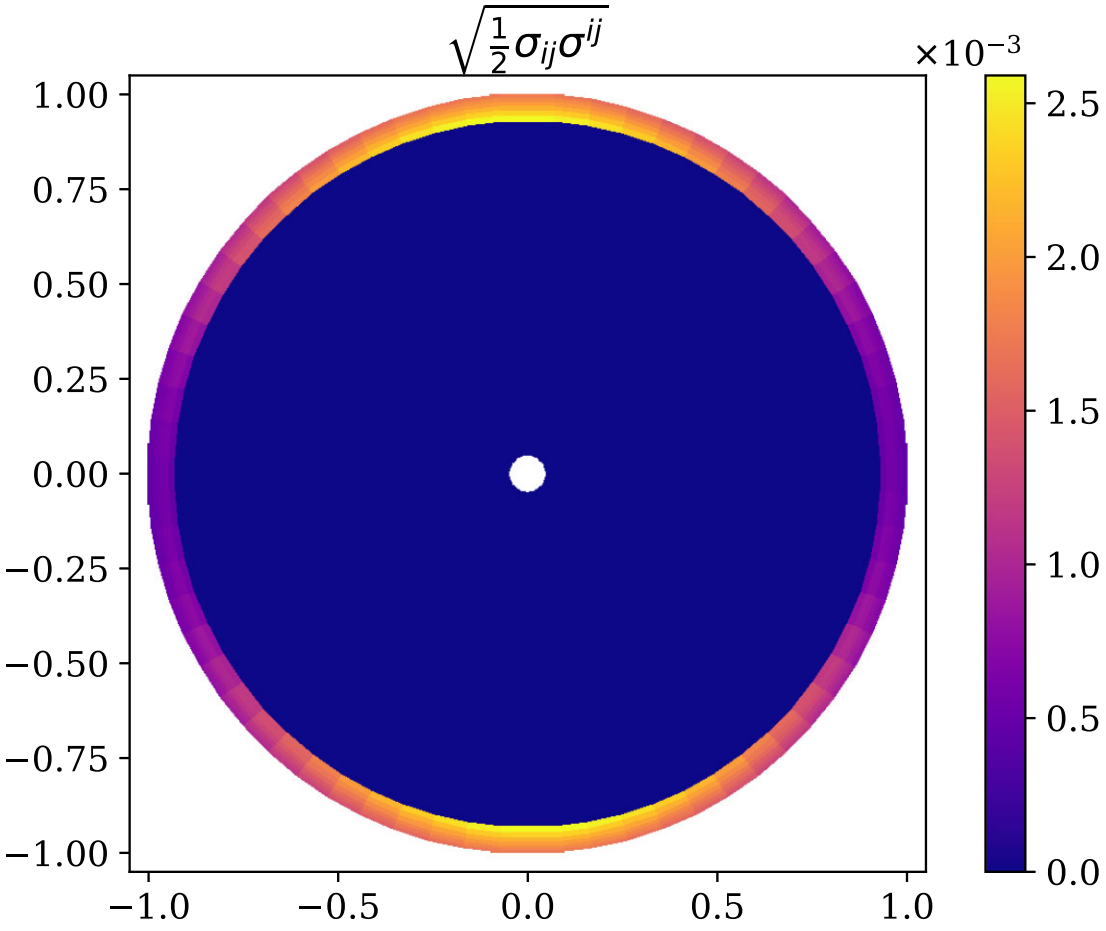

Figure 16. NS crust strain after 167 Myr, shown in a meridional cut.

(0.2 dimensionless time). The azimuthal magnetic field reaches saturation around 20 Myr. The instability induces strong electric current in the NS crust and leads to exponential decay of magnetic energy on a time-scale of 60 Myr in our setup with initial $B_r = 10^{14}$ G at the pole.

Our work has the following potential astrophysical implications:

(i) We found that ambipolar diffusion creates electric currents in the deep crust and allows energy release at the level of 10^{29} erg s^{-1} on a 10 Myr time-scale. Thus an NS could stay relatively hot with temperatures of $\approx 10^5$ K for millions of years if it had a strong initial magnetic field $\approx 10^{14}$ G. NSs with these temperatures were discovered in the past using optical, UV, and X-ray telescopes. Future missions such as the Large UV/Optical/IR Surveyor (LUVOIR; The LUVOIR Team 2019) as well as the next generation of X-ray telescopes such as Strobe-X (Ray et al. 2019) could be used to measure surface temperatures for large number of old neutron stars and confirm or reject our numerical results. More work is required to produce reliable surface maps which will be possible to compare with UV and soft X-ray light curves.

(ii) In our simulations, the dipolar component of magnetic field decays on a time-scale of 120 Myr, which is expected to be sensitive to the conductivity of the deep crust. Further numerical simulations are required to establish a firm relationship between decay time-scale, initial magnetic field strength and configuration, and conductivity of the deep crust. Ultimately, these decay time-scales will be used in pulsar population synthesis to decode evolutionary relations between different classes of neutron stars (such as magnetars, central compact objects, radio pulsars, and dim isolated X-ray sources).

(iii) The instability leads to development of azimuthal magnetic field with initial wavenumber $m = 14$ which merges with time and simplifies its structure reaching $m = 4$ by 160 Myr. Many old radio pulsars continue to operate below the classical death line for dipolar magnetic field (Medin & Lai 2007). If ambipolar diffusion operates in these stars, it could be an important mechanism to increase the curvature of open field lines near the crust and facilitate the pair production allowing an NS to shine as a radio pulsar.

(iv) Ambipolar diffusion does not seem to cause any crust failure for magnetic field 10^{14} G.

ACKNOWLEDGEMENTS

AIP thanks Dr. Girish Nivarti, Dr. Anna Guseva, and Dr. Calum Skene for multiple fruitful discussions. AIP was very grateful to the `Dedalus` developers for fast and helpful support. This work was supported by STFC grant no. ST/W000873/1, and was undertaken on ARC4, part of the High Performance Computing facilities at the University of Leeds, UK.

DATA AVAILABILITY

The data underlying this article will be shared on reasonable request to the corresponding author.

REFERENCES

Akgün T., Reisenegger A., Mastrano A., Marchant P., 2013, MNRAS, 433, 2445
Alpar M. A., Cheng A. F., Ruderman M. A., Shaham J., 1982, Nature, 300, 728
Anzuini F., Melatos A., Dehman C., Viganò D., Pons J. A., 2022, MNRAS, 515, 3014
Ascher U. M., Ruuth S. J., Spiteri R. J., 1997, Appl. Num. Math., 25, 151
Bhattacharya D., van den Heuvel E. P. J., 1991, Phys. Rep., 203, 1
Bilous A. V. et al., 2019, ApJ, 887, L23
Burns K. J., Vasil G. M., Oishi J. S., Lecoanet D., Brown B. P., 2020, Phys. Rev. Res., 2, 023068
Castillo F., Reisenegger A., Valdivia J. A., 2017, MNRAS, 471, 507
Castillo F., Reisenegger A., Valdivia J. A., 2020, MNRAS, 498, 3000
Cruces M., Reisenegger A., Tauris T. M., 2019, MNRAS, 490, 2013
De Grandis D., Turolla R., Wood T. S., Zane S., Taverna R., Gourgouliatos K. N., 2020, ApJ, 903, 40
De Grandis D., Taverna R., Turolla R., Gnarini A., Popov S. B., Zane S., Wood T. S., 2021, ApJ, 914, 118
Dommes V. A., Gusakov M. E., 2017, MNRAS, 467, L115
Elfritz J. G., Pons J. A., Rea N., Glampedakis K., Viganò D., 2016, MNRAS, 456, 4461
Glampedakis K., Andersson N., Samuelsson L., 2011, MNRAS, 410, 805
Goldreich P., Reisenegger A., 1992, ApJ, 395, 250
Gourgouliatos K. N., Cumming A., 2014, MNRAS, 438, 1618
Gourgouliatos K. N., Cumming A., 2015, MNRAS, 446, 1121
Gourgouliatos K. N., Hollerbach R., 2018, ApJ, 852, 21
Gourgouliatos K. N., Cumming A., Reisenegger A., Armaza C., Lyutikov M., Valdivia J. A., 2013, MNRAS, 434, 2480
Gourgouliatos K. N., Wood T. S., Hollerbach R., 2016, Proc. Natl. Acad. Sci., 113, 3944
Gourgouliatos K. N., Hollerbach R., Igoshev A. P., 2020, MNRAS, 495, 1692
Gourgouliatos K. N., De Grandis D., Igoshev A., 2022, Symmetry, 14, 130
Graber V., Andersson N., Glampedakis K., Lander S. K., 2015, MNRAS, 453, 671
Harding A. K., 2013, Front. Phys., 8, 679
Hoffman K., Heyl J., 2012, MNRAS, 426, 2404
Hollerbach R., Rüdiger G., 2002, MNRAS, 337, 216
Hollerbach R., Rüdiger G., 2004, MNRAS, 347, 1273
Hoyos J., Reisenegger A., Valdivia J. A., 2008, A&A, 487, 789
Igoshev A. P., 2019, MNRAS, 482, 3415
Igoshev A. P., Elfritz J. G., Popov S. B., 2016, MNRAS, 462, 3689
Igoshev A. P., Hollerbach R., Wood T., Gourgouliatos K. N., 2021a, Nat. Astron., 5, 145
Igoshev A. P., Popov S. B., Hollerbach R., 2021b, Universe, 7, 351
Igoshev A. P., Gourgouliatos K. N., Hollerbach R., Wood T. S., 2021c, ApJ, 909, 101
Kaspi V. M., Beloborodov A. M., 2017, ARA&A, 55, 261
Lander S. K., Andersson N., Antonopoulou D., Watts A. L., 2015, MNRAS, 449, 2047
Lecoanet D., Vasil G. M., Burns K. J., Brown B. P., Oishi J. S., 2019, J. Comput. Phys. X, 3, 100012
Lorimer D. R., Kramer M., 2012, Handbook of Pulsar Astronomy. Cambridge Univ. Press, Cambridge, UK
Markey P., Tayler R. J., 1973, MNRAS, 163, 77
Mayer M. G. F., Becker W., 2021, A&A, 651, A40
Medin Z., Lai D., 2007, MNRAS, 382, 1833
Mignani R. P., Pavlov G. G., Kargaltsev O., 2008, A&A, 488, 1027
Mises R. v., 1913, Mechanik der festen K'orper im plastisch- deformablen Zustand. Available at: https://www.digizeitschriften.de/id/252457811_1913
Oppenheimer J. R., Volkoff G. M., 1939, Phys. Rev., 55, 374
Passamonti A., Akgün T., Pons J. A., Miralles J. A., 2017, MNRAS, 465, 3416
Pavlov G. G., Kargaltsev O., Wong J. A., Garmire G. P., 2009, ApJ, 691, 458
Pearson J. M., Chamel N., Potekhin A. Y., Fantina A. F., Ducoin C., Dutta A. K., Goriely S., 2018, MNRAS, 481, 2994
Pons J. A., Viganò D., 2019, Living Rev. Comput. Astrophys., 5, 3
Pons J. A., Miralles J. A., Geppert U., 2009, A&A, 496, 207
Ray P. S. et al., 2019, preprint (arXiv:1903.03035)
Ruderman M., 1969, Nature, 223, 597
Sawyer R. F., 1989, Phys. Rev. D, 39, 3804
Shabaltas N., Lai D., 2012, ApJ, 748, 148
Tayler R. J., 1973, MNRAS, 161, 365
The LUVOIR Team, 2019, preprint (arXiv:1912.06219)
Turolla R., 2009, in Becker W., ed., Astrophysics and Space Science Library, Vol. 357, Neutron Stars and Pulsars. Springer-Verlag, Berlin, p. 141
Vasil G. M., Lecoanet D., Burns K. J., Oishi J. S., Brown B. P., 2019, J. Computat. Phys. X, 3, 100013
Viganò D., Pons J. A., 2012, MNRAS, 425, 2487
Viganò D., Rea N., Pons J. A., Perna R., Aguilera D. N., Miralles J. A., 2013, MNRAS, 434, 123
Wareing C. J., Hollerbach R., 2009, Phys. Plasmas, 16, 042307
Wareing C. J., Hollerbach R., 2010, J. Plasma Phys., 76, 117
Wood T. S., Graber V., 2022, Universe, 8, 228
Yakovlev D. G., Shalybkov D. A., 1990, Sov. Astron. Lett., 16, 86

APPENDIX A: DERIVATION OF THE EQUATION FOR CHEMICAL EQUILIBRIUM DEVIATION

We start with the same system of equations as Passamonti et al. (2017):

$$-\vec{\nabla}\mu_p - m_p^*\vec{\nabla}\Phi + e\left(\vec{E} + \frac{\vec{v}_p}{c}\times\vec{B}\right) = \frac{m_p^*\vec{w}_{pn}}{\tau_{pn}} + \frac{m_p^*\vec{w}_{pe}}{\tau_{pe}},$$
$$-\vec{\nabla}\mu_e - m_e^*\vec{\nabla}\Phi - e\left(\vec{E} + \frac{\vec{v}_e}{c}\times\vec{B}\right) = \frac{m_e^*\vec{w}_{en}}{\tau_{en}} + \frac{m_e^*\vec{w}_{ep}}{\tau_{ep}},$$
$$-\vec{\nabla}\mu_n - m_n^*\vec{\nabla}\Phi = \frac{m_n^*\vec{w}_{np}}{\tau_{np}} + \frac{m_n^*\vec{w}_{ne}}{\tau_{ne}},$$

where μ_p, μ_e, and μ_n are chemical potentials for protons, electrons, and neutrons, Φ is the gravitational potential, $m_{\rm p}^*$, $m_{\rm n}^*$, and $m_{\rm e}^*$ are effective masses of proton, neutron, and electron, respectively. Absolute velocities for different species are $\vec{v}_{\rm p}$ and $\vec{v}_{\rm e}$, while relative velocities between species are $\vec{w}_{\rm pe} = \vec{v}_{\rm p} - \vec{v}_{\rm e}$. Here, $\tau_{\rm pn}$ are relaxation times for collisions between protons and neutrons. This system contains one more equation in comparison to Goldreich & Reisenegger (1992) for motion of neutrons which are not fixed.

We add the first two equations and subtract the third equation:

$$-\nabla(\Delta\mu) - \vec{\nabla}\Phi(m_{\rm p}^* + m_{\rm e}^* - m_{\rm n}^*) + \frac{\vec{j}\times\vec{B}}{cn_c} = \frac{m_{\rm p}^*\vec{w}_{\rm pn}}{\tau_{\rm pn}} - \frac{m_{\rm n}^*\vec{w}_{\rm np}}{\tau_{\rm np}}. \tag{A1}$$

In this equation, we combine $\Delta\mu = \mu_p + \mu_e - \mu_n$. The right-hand side does not contain any terms with $\vec{w}_{\rm pe}$ because of conservation of momentum, so $n_{\rm p}m_{\rm p}^*/\tau_{\rm pe} = n_{\rm e}m_{\rm e}^*/\tau_{\rm ep}$ and $\vec{w}_{\rm pe} = -\vec{w}_{\rm ep}$, and electroneutrality $n_{\rm e} \approx n_{\rm p} = n_{\rm c}$. Following Passamonti et al. (2017) we assume that electron–neutron interactions are much weaker in comparison to proton–neutron interactions which are mediated by the strong force. That is why we neglected terms with $\tau_{\rm en}$ and $\tau_{\rm ne}$. We also assume that contribution of electrons to NS mass is negligible, i.e. $m_{\rm p}^* + m_{\rm e}^* - m_{\rm n}^* \approx 0$. We combine the terms on the right as follows:

$$\frac{m_{\rm p}^*\vec{w}_{\rm pn}}{\tau_{\rm pn}} - \frac{m_{\rm n}^*\vec{w}_{\rm np}}{\tau_{\rm np}} = \frac{m_{\rm p}^*\vec{w}_{\rm pn}}{\tau_{\rm pn}} + \frac{n_{\rm p}}{n_{\rm n}}\frac{m_{\rm p}^*\vec{w}_{\rm pn}}{\tau_{\rm pn}} = \frac{m_{\rm p}^*\vec{w}_{\rm pn}}{x_{\rm n}\tau_{\rm pn}}, \tag{A2}$$

where $x_{\rm n} = n_{\rm n}/(n_{\rm p} + n_{\rm n})$. Overall, at this stage we have the following equation:

$$-\nabla(\Delta\mu) + \frac{\vec{f}_B}{n_c} = \frac{m_{\rm p}^*\vec{w}_{\rm pn}}{x_{\rm n}\tau_{\rm pn}}, \tag{A3}$$

where we define:

$$\vec{f}_B = \frac{\vec{j}\times\vec{B}}{c} = \frac{1}{4\pi}(\vec{\nabla}\times\vec{B})\times\vec{B}. \tag{A4}$$

We take the divergence of equation (A3) and multiply by (-1):

$$\vec{\nabla}^2(\Delta\mu) = \vec{\nabla}\cdot\left(\frac{\vec{f}_B}{n_c}\right) - \vec{\nabla}\cdot\left(\frac{m_{\rm p}^*\vec{w}_{\rm pn}}{x_{\rm n}\tau_{\rm pn}}\right). \tag{A5}$$

We expand the last term on the right, multiplying numerator and denominator by $n_{\rm c}$:

$$\vec{\nabla}\cdot\left(\frac{m_{\rm p}^*\vec{w}_{\rm pn}}{x_{\rm n}\tau_{\rm pn}}\right) = \frac{m_{\rm p}^*}{x_{\rm n}n_c\tau_{\rm pn}}\vec{\nabla}\cdot(n_c\vec{w}_{\rm pn}) + n_c\vec{w}_{\rm pn}\cdot\vec{\nabla}\left(\frac{m_{\rm p}^*}{x_{\rm n}n_c\tau_{\rm pn}}\right). \tag{A6}$$

Following the assumption by Passamonti et al. (2017), we similarly assume:

$$\vec{\nabla}\cdot(n_c\vec{w}_{\rm pn}) = -\frac{\lambda\Delta\mu}{x_{\rm n}}. \tag{A7}$$

Further we substitute $n_c\vec{w}_{\rm pn}$ from equation (A3) into equation (A6):

$$n_c\vec{w}_{\rm pn} = \frac{x_{\rm n}\tau_{\rm pn}n_c}{m_{\rm p}^*}\left(-\vec{\nabla}(\Delta\mu) + \frac{\vec{f}_B}{n_c}\right). \tag{A8}$$

Thus, the final equation is written as

$$\vec{\nabla}^2(\Delta\mu) - \frac{m_{\rm p}^*\lambda}{x_{\rm n}^2n_{\rm c}\tau_{\rm pn}}\Delta\mu = \vec{\nabla}\cdot\left(\frac{\vec{f}_B}{n_{\rm c}}\right) - \frac{x_{\rm n}\tau_{\rm pn}n_{\rm c}}{m_{\rm p}^*}\left(-\vec{\nabla}(\Delta\mu) + \frac{\vec{f}_B}{n_{\rm c}}\right)\vec{\nabla}\cdot\left(\frac{m_{\rm p}^*}{x_{\rm n}n_{\rm c}\tau_{\rm pn}}\right). \tag{A9}$$

APPENDIX B: VERIFICATION OF THE CODE AND CHOICE OF NUMERICAL RESOLUTION

Comparing our short simulations for a range of temperatures (see Fig. 5) we notice that while the solution for $\Delta\mu$ looks very similar to Fig. 3 in Passamonti et al. (2017), our amplitude is approximately three times larger. The exact reason for this difference is unknown. Our guess is that the difference appears because we normalize the equations differently. In the absence of open-source code used by Passamonti et al. (2017),

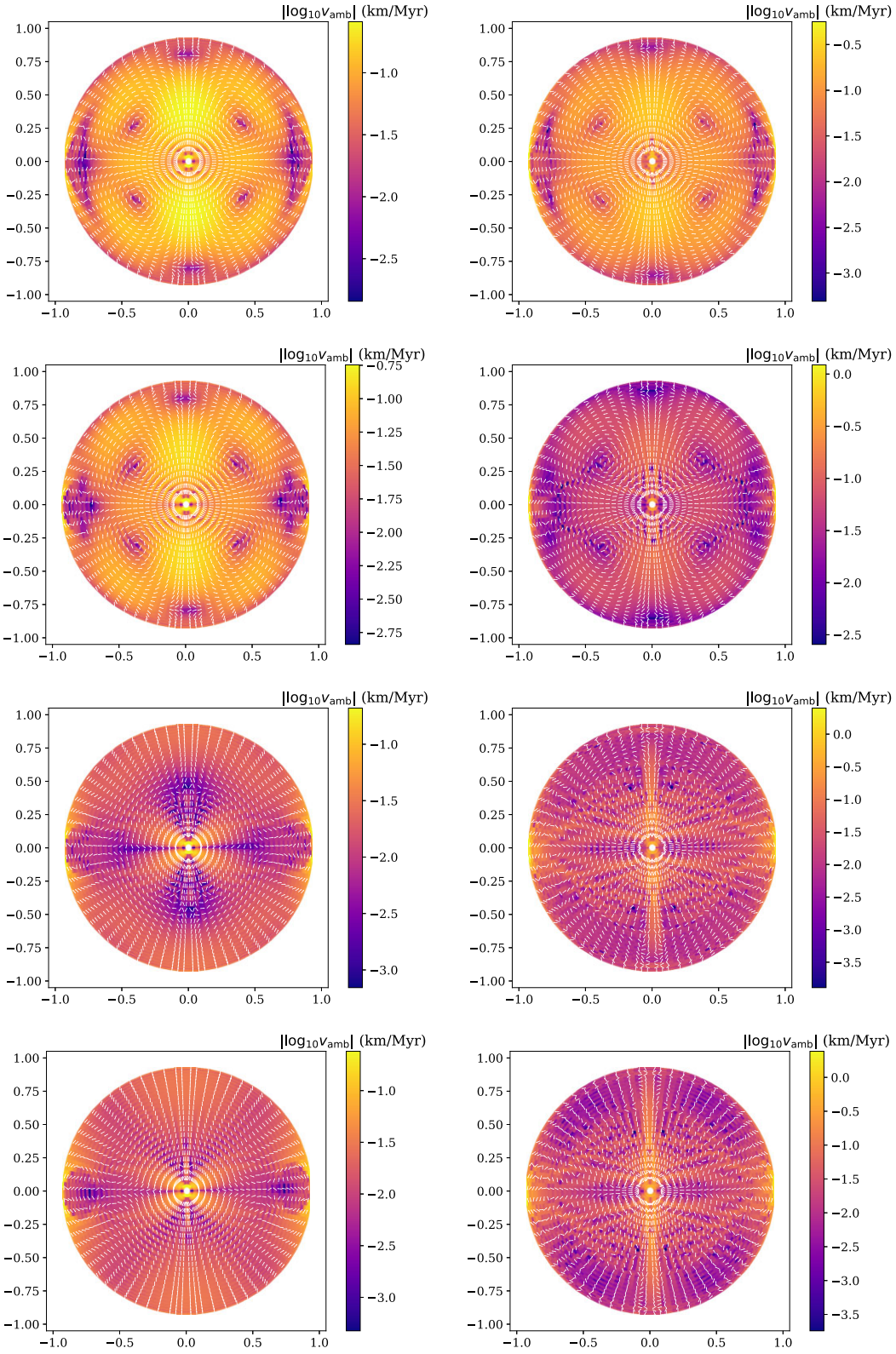

Figure B1. Evolution of speed of ambipolar diffusion with fixed temperature $T_8 = 1$ and $r_{\rm cut} = 2$ for ξ_3, ξ_4 (left column) and no $r_{\rm cut}$ (right column). From top to bottom the four rows are at ages 4 Kyr, 10 Kyr, 400 Kyr, and 1.5 Myr.

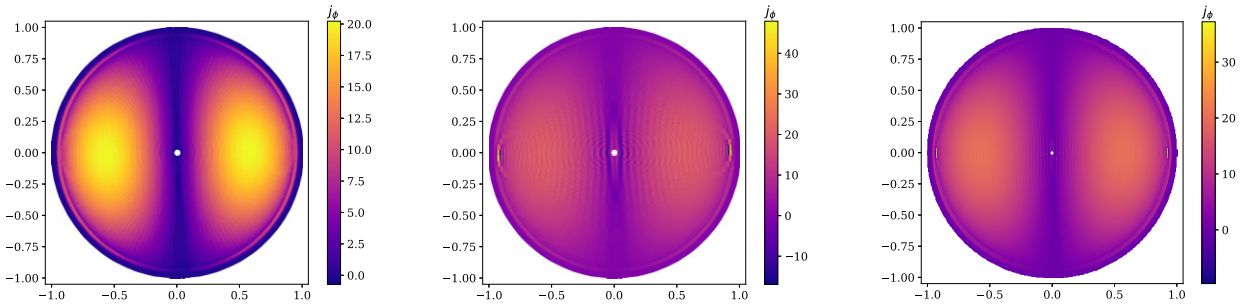

Figure B2. Left-hand panel: electric current j_ϕ at 600 Kyr in simulations with $r_{\rm cut} = 2$. Middle and right-hand panels: no restriction on ξ_3, ξ_4 for resolution B (middle panel) and for resolution D (right-hand panel).

the difference is nearly impossible to track. Despite this difference in amplitude we successfully reproduce the ambipolar velocity speeds and its patterns. In all our simulations $\Delta\mu/\mu_0 \ll 1$ which justifies application of linear approximation for reaction rates. With the cooling of the NS when temperature drops from $T_9 = 1$ to $T_9 = 0.1$ the velocity pattern transforms from irrotational-dominated flow to solenoidal-dominated flow in agreement with Passamonti et al. (2017). We successfully reproduce the location of zeros in this flow pattern.

We notice that radial profiles for ξ_3 and ξ_4 span many orders of magnitude from NS centre to the core–crust boundary. Passamonti et al. (2017) remarked that parameter b, see equation (38), is measured in km and decays towards the core–crust interface reaching values around 200 m. Although our resolution is sufficient to resolve structures with size ≈50 m in radial direction at the core–crust boundary, we do not seem to resolve the process completely. This is the motivation for introducing the parameter $r_{\rm cut}$ which restricts the maximum value reached by ξ_3 and ξ_4.

We show the result of our simulations in Fig. B1. While the velocity field stays mostly smooth in the case of $r_{\rm cut} = 2$ (left-hand panel), small-scale noise-like structures emerge if no cut is imposed (right-hand panel). The rise of these structures coincides with appearance of a strong current at the core–crust boundary near $\theta = 90^\circ$, see Fig. B2 for details. It is clear from this figure that large values of ξ_3 and ξ_4 cause appearance of compact current (see middle and right-hand panels of Fig. B1). When we increase the numerical resolution the size of this current decays, but is still not fully resolved even with resolution D. It is to avoid these probable numerical artefacts that we introduced $r_{\rm cut} = 2$ in our basic simulations. When we introduce this restriction currents are well resolved and the velocity field looks much smoother.

In order to check that behaviour which we identified in our simulation is actual physical behaviour and not a problem of the code, we run shorter simulations with different numerical resolution and varying parameter $r_{\rm cut}$. We demonstrate the results of these simulations in Fig. B3. A field with similar structure emerges in simulations with $r_{\rm cut} = 20$ and better radial resolution. This toroidal magnetic field reaches maxima at radial distance of $r \approx 0.8\ {\rm R_{NS}}$, i.e. well below the crust. When we increase the numerical resolution even further and removed restriction on radial profiles ξ_3 and ξ_4 we notice that a very similar toroidal magnetic field is formed. It requires significant computational resources to evolve simulation with resolution D on time-scales of 10–20 Myr.

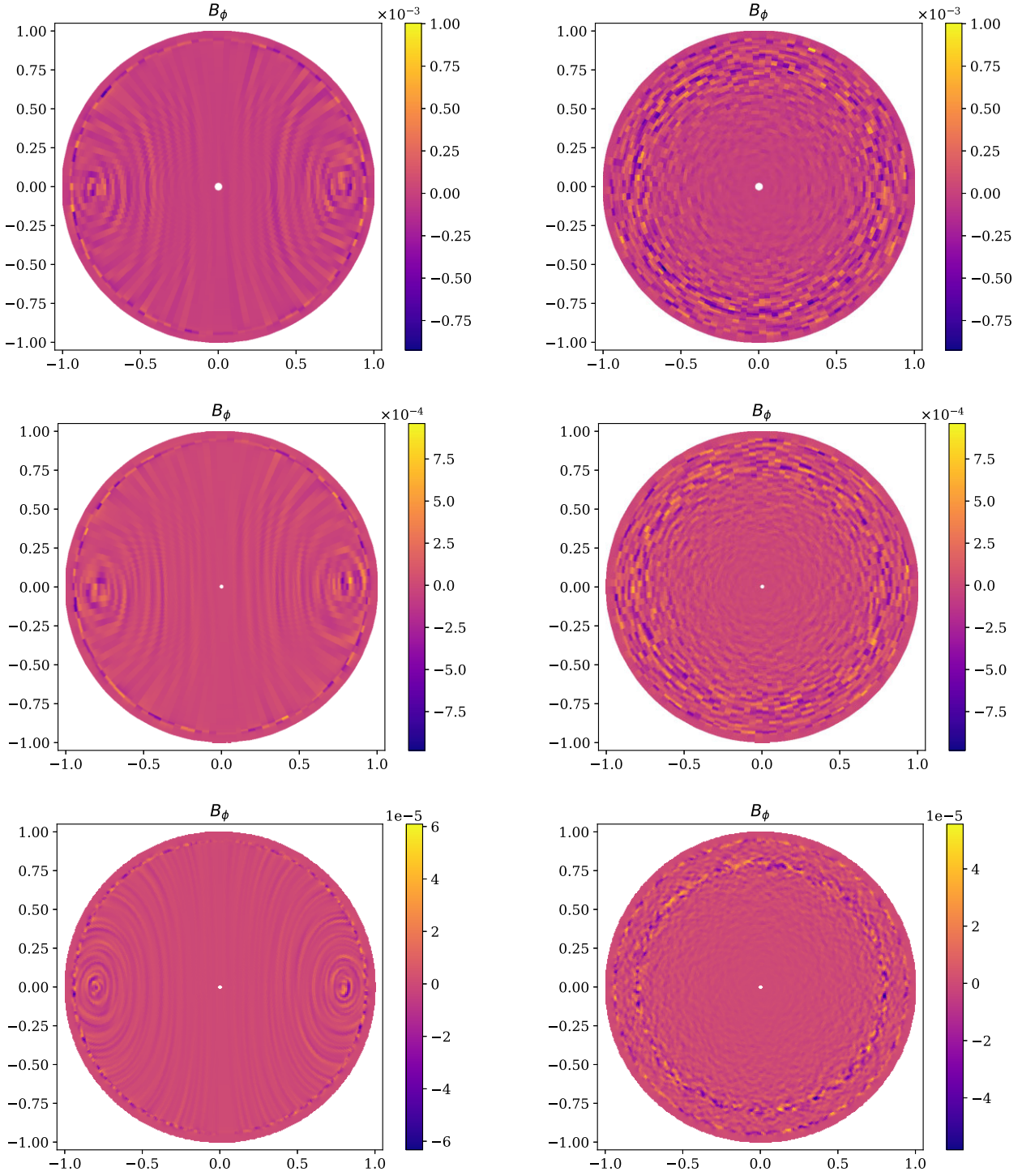

Figure B3. Formation of regular non-axisymmetric toroidal magnetic field. The left column shows meridional cuts, the right column shows equatorial cuts, with times at 100 Kyr. The top row shows the results of simulations with resolution B and $r_{\rm cut} = 2$. The middle row shows the results of simulations with resolution C and $r_{\rm cut} = 20$. The last row shows the results of simulations with resolution D and no $r_{\rm cut}$ imposed.

APPENDIX C: DERIVATION OF THE INITIAL CONDITION FOR VECTOR POTENTIAL

The initial condition by Akgün et al. (2013) is written for poloidal and toroidal magnetic fields and not for their potentials. Namely, Akgün et al. (2013) writes the magnetic field as

$$\vec{b} = \hat{\nabla}\alpha \times \hat{\nabla}\phi + \beta\hat{\nabla}\phi, \tag{C1}$$

while the standard poloidal–toroidal decomposition is:

$$\vec{b} = \vec{\nabla} \times \vec{\nabla} \times (b_{\rm p}\hat{r}) + \vec{\nabla} \times (b_t \hat{r}). \tag{C2}$$

Here $\hat{\nabla}\phi = \hat{\phi}/(r \sin\theta)$ and:

$$\alpha = f(x) \sin^2\theta, \tag{C3}$$

where $f(x)$ could be written as

$$f(x) = \frac{35}{8}x^2 - \frac{21}{4}x^4 + \frac{15}{8}x^6. \tag{C4}$$

Here, $x = r \in (0, 1]$. The respective scalar field for toroidal component is written as

$$\beta = \begin{cases} (\alpha - 1)^2 & \text{for } \alpha \geq 1, \\ 0 & \text{for } \alpha < 1. \end{cases} \tag{C5}$$

First, we consider only the poloidal part of the magnetic field. We transform the first term of equation (C1) and write it as

$$\vec{b}_{\rm p} = \vec{\nabla} \times (\alpha \vec{\nabla}\phi). \tag{C6}$$

In this case we just need to find b_p such that $\vec{\nabla} \times (b_{\rm p}\hat{r}) = \alpha\vec{\nabla}\phi$. Expanding the curl and assuming that the initial condition is axisymmetric we obtain:

$$-\frac{1}{r}\frac{\partial b}{\partial \theta} = \alpha \nabla\phi = \frac{f(x)}{r\sin\theta}\sin^2\theta, \tag{C7}$$

using the same radial function $f(x)$ as by Akgün et al. (2013). The equation (C7) can be solved if we assume:

$$b_{\rm p}(r, \theta) = f(r)\cos\theta. \tag{C8}$$

The same initial condition can also be written in terms of vector potential $\vec{A}$:

$$\vec{\nabla} \times \vec{A} = \vec{B} = \vec{\nabla} \times \left[(b_t\vec{r}) + \vec{\nabla} \times (b_{\rm p}\vec{r})\right], \tag{C9}$$

which we can write in components of the vector potential:

$$\begin{aligned} A_r &= b_t, \\ A_\theta &= \left[\vec{\nabla} \times (b_{\rm p}\vec{r})\right]_\theta, \\ A_\phi &= \left[\vec{\nabla} \times (b_{\rm p}\vec{r})\right]_\phi. \end{aligned} \tag{C10}$$

In our case:

$$\begin{aligned} A_r &= 0, \\ A_\theta &= 0, \\ A_\phi &= \tfrac{f(r)}{r}\sin\theta. \end{aligned} \tag{C11}$$

If we next add the toroidal magnetic field:

$$\beta\frac{\hat{\phi}}{r\sin\theta} = \nabla \times (b_t\vec{r}), \tag{C12}$$

then expanding the curl we obtain:

$$\frac{\partial b_t}{\partial\theta} = \frac{\beta}{\sin\theta}. \tag{C13}$$

We can solve this differential equation for cases when $\alpha \geq 1$:

$$b_t = \frac{1}{12}\left(\cos(3\theta) - 9\cos(\theta)\right) f^2(x) - 2f(x)\cos\theta + \log\left(\cot\left[\frac{\theta}{2}\right]\right). \tag{C14}$$

For the cases $\alpha < 1$ we have to use a correct constant.

This paper has been typeset from a TEX/LATEX file prepared by the author.